

Parity nonconservation in the hydrogen atom. III

L. P. Lévy* and W. L. Williams

Harrison M. Randall Laboratory, University of Michigan, Ann Arbor, Michigan 48109

(Received 14 October 1983)

We obtain an upper limit on the electron vector—proton axial vector weak-coupling constant, C_{2p} , of 620, using the parity-odd signature of weak-induced interferences in a microwave transition rate in $H(2S)$. Several powerful techniques, based on the analysis of resonance line shapes, allow us to detect the presence of interference processes and understand their nature. They permit us to sort out and accurately eliminate systematic effects and to extract residual parity-nonconserving contributions to the transition rate. We extend the well-known method of invariant analysis to time-dependent situations and relate it to line-shape theory. Because of their analytical nature, the results obtained lend themselves well to the precise description of experimental line shapes and should have application in other research areas.

I. INTRODUCTION

The unified gauge model of electroweak interactions¹ has successfully explained most of the relevant high-energy particle-physics experiments, and the recent discoveries of the gauge bosons, W^\pm and Z^0 ,² have confirmed the current picture. Because of several theoretical difficulties, it is of interest to investigate the behavior of electroweak processes at very low (atomic physics) and very high energies, where the presence of other gauge particles as well as higher-order “radiative corrections” could play an important role.³

The electron-nucleon sector of electroweak theories can be parametrized in terms of four dimensionless coupling constants denoted by C_{1p} (electron axial vector—proton vector, $A_e - V_p$), C_{2p} ($V_e - A_p$), and the corresponding ones for the electron and neutron, C_{1n} and C_{2n} .⁴ Atomic-physics experiments should provide, through precision measurements of these constants, a significant test of the unified theory of weak and electromagnetic interactions at zero momentum transfer.

Parity-nonconserving (PNC) forces induce small but significant mixings of close-lying parity doublets in hydrogenic systems, which can be measured experimentally.⁵ This work reports a limit on C_{2p} obtained in an experiment carried out with a beam of metastable ($2S$) hydrogen. The experiment relies on the natural separation of the weak-coupling constants at the different level crossings which occur in the $n=2$ shell. The general ideas underlying this experiment are briefly described in Sec. II with reference to prior work. We stress the methods developed for this work since they are of greater scientific interest than the limit on C_{2p} obtained. They consist of extending the invariant decomposition of transition rates (Sec. III) to time-dependent situations and relating each invariant to a characteristic line-shape distortion of the transition probability (Sec. IV). Since the line shapes of the Stark-induced transitions used in the experiment are known analytically (Sec. IV), we are able to obtain in Sec. V the distortion of the resonance line for the most significant systematic effects in analytic form. The field distri-

butions experienced by atoms in the beam are known and this permits us to derive the transition line shapes averaged over the geometry of the beam. Detailed predictions of the dependence of the systematic effects on the beam position and divergence as well as their dependence on field strengths are obtained from this analysis. All these predictions have been borne out by the experiment, described in Sec. VI, and, in particular, we have verified the dynamical role of the relative widths of the initial and final states. The methods described in this work have enabled us to understand the observed line shapes at a level of one part in 10^3 and can presumably be applied to many other experimental situations.

II. DESCRIPTION OF THE EXPERIMENT

Our experiments use atoms in the $n=2$ state of hydrogen wherein there is the close-lying long-lived $2S_{1/2}$

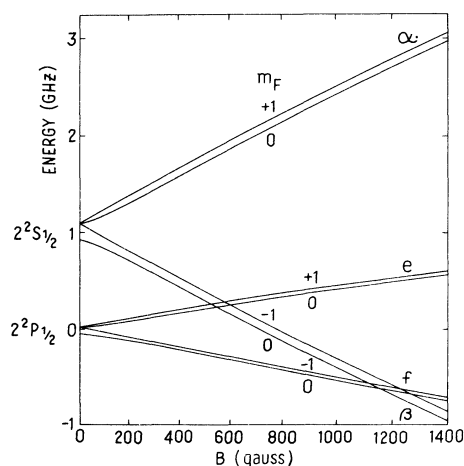


FIG. 1. Zeeman diagram of the $2^2P_{1/2}$ and $2^2S_{1/2}$ states of hydrogen.

short-lived $2P_{1/2}$ parity doublet (Fig. 1). We employ external electric and magnetic fields. The Zeeman effect is used to reduce the energy denominator in the weak mixing amplitude by a factor of ≈ 20 , the ratio of the Lamb shift to the $2P$ radiation width, to enhance the mixing. From Fig. 1 it is seen that there are two values of the magnetic field where the $2S$ and $2P$ Zeeman substates cross, near 575 and 1190 G. Selection rules for the mixing result in essentially only the electron axial vector—proton vector coupling, parametrized by the constant C_{2p} , entering at the lower field crossing, while this coupling, as well as the electron vector—proton axial vector coupling with associated coupling constant C_{1p} , enter at the higher field crossing. We are at present focusing on the measurement of C_{2p} near the lower field crossing. By applying a dc electric field to mix the $2^2S_{1/2}$ and $2^2P_{1/2}$ states via the Stark effect, we induce a (parity-conserving) PC electric dipole transition moment which permits driving microwave electric dipole transitions between perturbed $2^2S_{1/2}$ hyperfine states (Fig. 1). The weak mixing similarly induces a PNC electric dipole transition moment. The transition rate is then

$$R = |A_{PC} + A_{PNC}|^2 \\ = |A_{PC}|^2 + (A_{PC}^* A_{PNC} + \text{c.c.}) + |A_{PNC}|^2, \quad (1)$$

where A_{PC} and A_{PNC} are, respectively, the PC and PNC transition electric dipole amplitudes. This technique results in an interference term which is linear in A_{PNC} . The sign of the interference term can be changed by inversions of the applied fields as our configuration of fields breaks inversion symmetry.

The specific hydrogen transition being observed is $\alpha_0(2S, m_J \cong +\frac{1}{2}, m_I \cong -\frac{1}{2})$ to $\beta_0(2S, m_J \cong -\frac{1}{2}, m_I \cong +\frac{1}{2})$ (~ 1600 MHz) in the vicinity of the β - e level crossing. The initial state α_0 was chosen because it has predominantly the opposite spin projections to β_0 , which helps suppress the PC Stark-induced amplitude with respect to the weak-induced amplitude. The detected final state is β_0 as it is the only state at this level crossing to be mixed with the nearby e_0 state by the PNC weak interaction.⁵

The arrangement of the fields in the transition region is shown schematically in Fig. 2. The static \vec{E} and \vec{B} fields

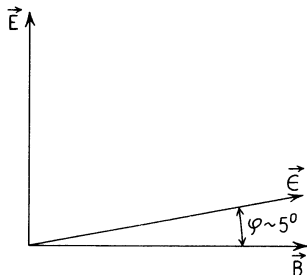


FIG. 2. Configuration of the fields in the transition region.

are orthogonal and the microwave electric field \vec{e} is tilted at a small angle φ relative to \vec{B} . This configuration is one which breaks inversion symmetry. In terms of invariant analysis of the rate, it gives rise to a pseudoscalar term proportional to $\vec{e} \cdot \vec{E} \vec{e} \cdot \vec{B}$ corresponding to the desired interference term.

The interference term changes sign under reversal of the direction of the dc electric field ($E_x \rightarrow -E_x$), reversal of the direction of the magnetic field ($\epsilon_z \rightarrow -\epsilon_z$), and a reversal of the angle between \vec{e} and the magnetic field ($\epsilon_x \rightarrow -\epsilon_x$). $|A_{PC}|^2$ is unchanged by these reversals. The amplitude A_{PC} is suppressed relative to A_{PNC} by three different factors. One factor, ϵ_x , is reduced by making the angle φ small. The factor $\sin\Theta$ expresses the residual mixing of m_J, m_I states by the hyperfine interaction. At the β_0 - e_0 crossing the states α_0 and β_0 have predominantly opposite signs of spin, with a small admixture ($\sim 6\%$) of the states with parallel spins. As electric dipole transitions do not change the proton spin, this additional factor suppresses A_{PC} . Finally, A_{PC} is suppressed by making E_x as small as is consistent with being limited by shot noise. We determine the asymmetry

$$A = \frac{R_+ - R_-}{R_+ + R_-} = 2 \left| \frac{A_{PNC}}{A_{PC}} \right| \cos\phi, \quad (2)$$

where R_{\pm} are the rates for the two choices of any one of the parameters which are inverted and ϕ is the relative phase of A_{PC} and A_{PNC} . The experimental parameters have been chosen to obtain a suppression of the α_0 - β_0 transition probability of 4 parts in 10^6 of the initial population. This yields a weak-induced asymmetry A of 3.8 parts in 10^6 for $C_{2p} = 1$. The contributions of the two strongly damped states e_{+1} and e_0 to the two amplitudes leads to a variable phase difference between the amplitudes as a function of magnetic field, and a difference in line shapes between the scalar and pseudoscalar terms. In the field configuration of our experiment the strong damping of the $2P$ state is requisite to obtaining the interference between the Stark and weak matrix elements which are relatively imaginary for a weak interaction which is T invariant.⁶

The general arrangement of the experiment is shown in Fig. 3. An intense beam of protons experiences resonant charge exchange to the $n=2$ state of atomic hydrogen. Subsequent state selection produces a beam polarized in the $\alpha(2^2S_{1/2}, m_J = +\frac{1}{2})$ hyperfine substates. The beam then enters the interaction region where we drive Stark-induced microwave electric dipole transitions between the α and β states in a magnetic field set near the β - e level crossing. This interaction region comprises the field configuration of Fig. 2, which has a sense of handedness. Because of the large velocity of the atomic beam, the dc elec-



FIG. 3. General experimental arrangement.

tric field \vec{E} in the rest frame of the atom was obtained by applying a small transverse magnetic field \vec{B}_T perpendicular to \vec{B}_0 , thereby ensuring the orthogonality of the motional electric field $\vec{E}=(\vec{v}/c)\times\vec{B}$ with $\vec{B}=\vec{B}_0+\vec{B}_T$. The presence of the β -state atoms resulting from the microwave transition is detected. The modification of the detector signal when the screw sense of the interaction region is accurately reversed is the signal resulting from the PNC interference term and comprises the measurement of the asymmetry (2). Two other allowed Stark-induced electric dipole transitions ($\alpha_0\rightarrow\beta_{-1}$, $\alpha_{+1}\rightarrow\beta_0$), 3 orders of magnitude larger than the $\alpha_0\rightarrow\beta_0$ transition, may also be driven in the interaction region. They are not sensitive to weak interactions and, as shown in Secs. III and IV, have systematic effects similar to those of the $\alpha_0\rightarrow\beta_0$ transition. Extensive reference to these calibration lines will be made throughout the paper, since they have been a powerful tool to check the integrity of the data.

III. TIME-INDEPENDENT INVARIANT ANALYSIS

It may not be straightforward to extract a PNC contribution to the transition rate as systematic PC contributions can, under particular circumstances, mimic PNC contributions. In order to understand such effects, we exploit the fact that PC contributions are scalar combinations of the physical variables which appear in the rate and PNC contributions are pseudoscalar combinations to carry out an invariant analysis of the rate.

As discussed above, the Stark-induced amplitudes for the suppressed $\alpha_0\rightarrow\beta_0$ transition, as well as the allowed calibration transitions ($\alpha_{+1}\rightarrow\beta_0$ and $\alpha_0\rightarrow\beta_{-1}$), result from the fields: \vec{e} , the microwave electric field; \vec{E} , the dc electric field; and \vec{B} , the dc magnetic field. The Stark-induced $\alpha\rightarrow\beta$ transition rates may be decomposed in terms of these three physical variables as^{7,8}

$$\begin{aligned} |A_S|^2 = & G_1(\vec{e}\times\hat{B})^2(\vec{E}\times\hat{B})^2 + G_2(\vec{e}\times\hat{B}\cdot\vec{E}\times\hat{B})^2 + G_3(\vec{e}\cdot\hat{B})^2(\vec{E}\times\hat{B})^2 + G_4(\vec{e}\times\hat{B})^2(\vec{E}\cdot\hat{B})^2 \\ & + G_5(\vec{e}\cdot\hat{B})^2(\vec{E}\cdot\hat{B})^2 + G_6(\vec{e}\cdot\hat{B})(\vec{E}\cdot\hat{B})(\vec{e}\times\hat{B}\cdot\vec{E}\times\hat{B}) \\ & + G_7(\vec{e}\cdot\hat{B})(\vec{E}\cdot\hat{B})(\vec{e}\times\vec{E}\cdot\hat{B}) + G_8(\vec{e}\times\hat{B}\cdot\vec{E}\times\hat{B})(\vec{e}\times\vec{E}\cdot\hat{B}). \end{aligned} \quad (3)$$

In the ideal configuration for our experiment $\vec{E}\cdot\hat{B}=0$ and \vec{e} , \vec{E} , and \vec{B} are coplanar, and three invariants remain in the Stark-induced rate:

$$\begin{aligned} |A_S|^2 = & G_1(\vec{e}\times\hat{B})^2(\vec{E}\times\hat{B})^2 + G_2(\vec{e}\times\hat{B}\cdot\vec{E}\times\hat{B})^2 \\ & + G_3(\vec{e}\cdot\hat{B})^2(\vec{E}\times\hat{B})^2, \end{aligned} \quad (4)$$

of which the first two occur in the rate for the $\alpha_0\rightarrow\beta_0$ transition.⁹

The $\alpha_0\rightarrow\beta_0$ transition rate involves pseudoscalar interference terms induced by the PNC weak interaction which are linear in \vec{E} :⁸

$$\begin{aligned} (A_S A_W^* + \text{c.c.}) = & J_1(\vec{e}\times\hat{B})^2(\vec{E}\cdot\hat{B}) + J_2(\vec{e}\cdot\hat{B})(\vec{e}\times\hat{B})\cdot(\vec{E}\times\hat{B}) \\ & + J_3(\vec{e}\cdot\hat{B})(\vec{e}\times\vec{E}\cdot\hat{B}) + J_4(\vec{e}\cdot\hat{B})^2(\vec{E}\cdot\hat{B}). \end{aligned} \quad (5)$$

For the ideal configuration, all the terms except the second vanish. For hydrogen and deuterium, the coefficients G , and the atomic structure contributions to the coefficients J , can be calculated to arbitrary precision as concerns the interpretation of our experiments. The invariant coefficients are functions of the magnetic field strength $|\vec{B}|$. In the vicinity of level crossings they exhibit widely different line shapes as the magnetic field is varied, a fact which will be exploited to aid in distinguishing a true pseudoscalar contribution to the transition rate from systematic effects.¹⁰

In the rest frame of the atom, the resultant dc electric field is $\vec{E}=\vec{E}_a+(\vec{v}/c)\times\vec{B}_0=\vec{E}_a+\vec{\beta}\times\vec{B}_0$, where \vec{E}_a , the applied motional field, is $\vec{\beta}\times\vec{B}_T$.⁷ The contribution of

the main Zeeman field \vec{B}_0 to the electric field \vec{E} may be quite sizeable in our fast beam even for small angles between \vec{v} and \vec{B}_0 . If the atomic beam axis is parallel to B_0 , this motional field, when averaged over the cross-sectional area of the beam, vanishes.¹¹

The discussion of the systematic effects will be restricted to the $\alpha_0\rightarrow\beta_0$ transition for which the invariants G_3 and G_4 do not appear. While we have yet to encounter problems from a stray electric field \vec{E} , a complete analysis for our future work must include such. To account for misalignment of the beam axis and/or beam divergence ($\vec{\beta}\times\vec{B}_0\neq 0$), we parametrize the relative orientation of $\vec{\beta}$ and \vec{B} with the angles¹² λ, χ shown in Fig. 4(a), with $\sin\lambda \ll 1$.

In the configuration used in the experiment, applied motional fields were used and $\vec{E}\times\vec{B}$ is identically zero. To account for misalignment of B_T ,¹³ we denote the x projection of B_T as $\sin\psi \ll 1$. We classify the systematic interference terms as to their symmetry properties under reversal of the directions of \vec{B}_T , or \vec{B}_0 , or $\varphi\rightarrow-\varphi$. The most significant systematic interference terms, that is, those suffering the least suppression under the reversals and proper alignment, are given in Table I, together with their dependences on the alignment angles.¹⁴ The most common terms arise from interference of microwave Stark amplitudes induced by the applied motional field and motional fields from beam misalignment and/or divergence with respect to \vec{B}_0 . These are odd under $\vec{B}_T\rightarrow-\vec{B}_T$, or $\vec{B}_0\rightarrow-\vec{B}_0$, and can be eliminated by careful alignment, together with the concomitant averaging over the atomic beam cross section.¹¹ The only field misalignment term of importance is that containing

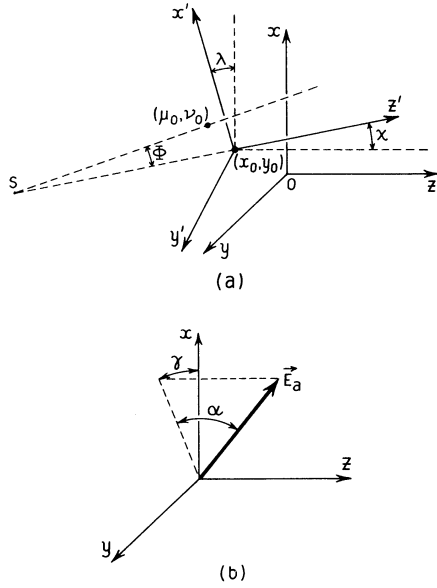


FIG. 4. (a) Laboratory and atomic beam coordinate frames. (b) Angles α, γ defining the direction of \vec{E}_a .

$\vec{\epsilon} \cdot \vec{B}_T \neq 0$. This term is also odd under reversal of the directions of \vec{B}_T and \vec{B}_0 . The largest systematic term is inherent to using an applied motional electric field. It results from modulation of the direction of the resultant magnetic field when $\vec{B}_T \rightarrow -\vec{B}_T$. It is odd under reversal of the direction of \vec{B}_T , but not under that of \vec{B}_0 . The terms arising from misalignments are all first-order suppressed in the alignment angles while the last term enjoys no such reduction. The terms with coefficient G_8 are formally odd under time reversal. All the terms listed in Table I have been observed in the $\alpha_0 \rightarrow \beta_0$ transition rate and confirm our analysis.

An alternative technique for obtaining \vec{E} with electrodes which extend through the microwave cavity has been recently developed. The resultant field is $\vec{E} = \vec{E}_a + \vec{\beta} \times \vec{B}_0$, and the large systematic effect resulting from modulation of the direction of the resulting magnetic field is absent. However, we must now include the possibility that $\vec{E}_a \cdot \vec{B}_0 \neq 0$. Here we classify systematic terms according to their symmetry properties under reversal of the directions of \vec{E}_a , or \vec{B}_0 , or $\varphi \rightarrow -\varphi$. We specify

misalignment of \vec{E}_a with respect to the x axis with angles α, γ [see Fig. 4(b)], where $\sin \alpha \ll 1, \sin \gamma \ll 1$. The most significant systematic interference terms are given in Table II. The first two terms arise from interference of Stark amplitudes induced by applied and motional electric fields while in the other three, the systematic Stark mixing results from stray electric fields. All the terms are odd under $\vec{E}_a \rightarrow -\vec{E}_a$ or $B_0 \rightarrow -B_0$; the second, third, and fourth terms are also odd under $\varphi \rightarrow -\varphi$. The terms involving motional fields are formally even under time reversal, and those involving stray fields are formally odd.

To illustrate the use of the analysis presented here, we compare the sensitivity to systematics of the $\alpha_0\beta_0$ and the $\alpha_0\beta_{-1}$ and $\alpha_{+1}\beta_0$ transition. Considering only motional electric fields $\vec{E} \cdot \hat{B} = 0$, the decomposition (1) and the selection rules give a single term

$$|A_S|^2 = G_3 (\vec{\epsilon} \cdot \hat{B})^2 (\vec{E} \times \hat{B})^2 \quad (6)$$

for the invariant decomposition of the calibration lines. For this case, the analysis of more subtle systematics (misalignments, time-dependent effects) is considerably simplified. This should be contrasted with the three terms

$$|A_S|^2 = G_1 (\vec{\epsilon} \times \hat{B})^2 (\vec{E} \times \hat{B})^2 + G_2 (\vec{\epsilon} \times \hat{B} \cdot \vec{E} \times \hat{B})^2 + G_8 (\vec{\epsilon} \times \hat{B} \cdot \vec{E} \times \hat{B}) (\vec{\epsilon} \times \vec{E} \cdot \hat{B}), \quad (7)$$

which arise for the $\alpha_0\beta_0$ transition. Close to the β - e level crossing, the two rates are quite similar, for G_1 is an order of magnitude larger than G_2 and G_8 . Thus all transitions are sensitive to the transverse electric field distribution E_{\perp} . On the other hand, the $\alpha_0\beta_0$ and the calibration transitions are sensitive, respectively, to the transverse (ϵ_{\perp}) and the longitudinal (ϵ_{\parallel}) microwave field distributions which in the central portion of the cavity are related by the tilt angle φ of the cavity axis with respect to \hat{B} . However, as a result of the cavity entrance and exit beam holes, the ratio $\epsilon_{\perp}/\epsilon_{\parallel}$ becomes quite nonuniform and appreciably larger at each end of the transition region than in the center. A thorough discussion of this effect can only be performed by analyzing the time-dependent behavior of a beam of finite extent through nonuniform fields. This analysis, carried out in Secs. IV and V, shows that the similarities between the $\alpha_0\beta_0$ and the calibration transitions goes far beyond the invariants (6) and (7); we will see that their line shapes are identical for weak fields.

TABLE I. Systematic interference terms with an applied motional electric field.

Source of systematic effect	Invariant form	Angular dependence
Beam misalignment and/or divergence	$2[(G_1 + G_2)/B^2](\vec{\epsilon} \times \vec{\beta} \cdot \vec{B}_0)(\vec{\epsilon} \times \vec{\beta} \cdot \vec{B}_T)$	$\cos \lambda \sin \chi \cos \gamma \cos \psi$
	$(-G_8/B)(\vec{\epsilon} \times \vec{\beta} \cdot \vec{B}_0)(\vec{\epsilon} \times \vec{B}_T) \cdot (\vec{\beta} \times \vec{B}_0)$	$\cos \lambda \sin \chi \cos \chi$
	$(-G_8/B)(\vec{\epsilon} \times \vec{\beta} \cdot \vec{B}_T)(\vec{\epsilon} \times \vec{B}_T) \cdot (\vec{\beta} \times \vec{B}_0)$	$\cos \lambda \sin \chi \cos \chi \cos^2 \psi$
Field misalignment	$(2G_1/B^2)(\vec{\beta} \times \vec{B}_T)^2 (\vec{\epsilon} \cdot \vec{B}_0)(\vec{\epsilon} \cdot \vec{B}_T)$	$\cos \chi \sin \psi$
Modulation of direction of \vec{B}	$(-G_8/B)(\vec{\epsilon} \times \vec{\beta} \cdot \vec{B}_T)(\vec{\epsilon} \times \vec{B}_T) \cdot (\vec{\beta} \times \vec{B}_T)$	$\cos \chi \cos \psi$

TABLE II. Systematic interference terms for an electric field applied with electrodes.

Source of systematic effect	Invariant form	Angular dependence
Beam misalignment and/or divergence	$2G_1(\vec{\epsilon} \times \hat{\mathbf{B}}_0 \cdot \vec{\mathbf{E}} \times \hat{\mathbf{B}}_0)(\vec{\epsilon} \times \vec{\beta} \cdot \vec{\mathbf{B}}_0)$	$\cos\lambda \sin\chi \cos\alpha \cos\gamma$
Beam misalignment and/or divergence and electric field misalignment	$G_6(\vec{\epsilon} \cdot \hat{\mathbf{B}}_0)(\vec{\mathbf{E}} \cdot \hat{\mathbf{B}}_0)(\vec{\epsilon} \times \vec{\beta} \cdot \vec{\mathbf{B}}_0)$	$\cos\lambda \sin\chi \sin\alpha$
Electric field misalignment and stray electric field	$G_7(\vec{\epsilon} \cdot \hat{\mathbf{B}}_0)(\vec{\mathbf{E}} \cdot \hat{\mathbf{B}}_0)(\vec{\epsilon} \times \vec{\beta} \cdot \vec{\mathbf{B}}_0)$	$\sin\alpha$
	$G_7(\vec{\epsilon} \cdot \hat{\mathbf{B}}_0)(\vec{\beta} \cdot \hat{\mathbf{B}}_0)(\vec{\epsilon} \times \vec{\mathbf{E}} \cdot \hat{\mathbf{B}}_0)$	$\cos\alpha \sin\gamma$
Stray field	$G_8(\vec{\epsilon} \times \hat{\mathbf{B}}_0) \cdot (\vec{\mathbf{E}} \times \hat{\mathbf{B}}_0)(\vec{\epsilon} \times \vec{\beta} \cdot \hat{\mathbf{B}}_0)$	$\cos\alpha \cos\gamma$

In conclusion, the symmetry properties of the transition rate allow us to separate the systematic effects from the weak interference term. The use of calibration lines allows us furthermore to align the fields so that a large number of systematics can be reduced to a very small level. Finally, the magnetic-field-dependent line shape can further discriminate a true PNC term from a spurious interference, because of the characteristic variation of the relative phase of the weak and Stark amplitudes through the β - e level crossings.

IV. TIME-DEPENDENT EFFECTS

Generally, in atomic beam experiments, the atoms interact with external fields during well-defined time periods as a result of spatial confinement of the fields. The response of the atoms to these fields has a characteristic time dependence determined, in part, by the atomic structure and, in part, by the spatial distribution of the fields. The observed line shapes of transitions between quantum states together with a knowledge of these distributions can provide a deep understanding of experimental results. In particular, the contributions to a resonance line shape from interference effects, such as those tabulated in Sec. II, can be unambiguously traced to a specific variation of the interaction between the atoms and the fields.

A. General theory

We use here a semiclassical approach by adding to a field-free Hamiltonian H_0 the classical coupling of the electron to the external time-dependent fields of definite amplitude and phase. The coupling with the radiation field is introduced in H_0 at the phenomenological level, $V(\vec{r}, t)$ is the interaction potential with all external perturbation as well as the weak Hamiltonian. If we denote by $|n\rangle$ and $\langle \tilde{m}|$ the left and right eigenvectors of H_0 , and λ_n^0 the eigenvalues, the wave equation may be written in the Schrödinger picture as

$$i\hbar \frac{d}{dt} a_n(t) = \lambda_n^0 a_n(t) + \sum_m \langle \tilde{n} | V(\vec{r}, t) | m \rangle a_m(t). \quad (8)$$

For small perturbations, as is the case in our experiment, we can solve (8) directly in an interaction picture. We use two such representations here.

The first is the Zeeman representation. The atoms in the parity experiment are neither prepared nor detected in field-free eigenstates but rather in eigenstates of the Zeeman Hamiltonian $H_Z = H_0 + \mu_0 \vec{\mathbf{B}} \cdot (g_L \vec{\mathbf{L}} + g_S \vec{\mathbf{S}} + g_I \vec{\mathbf{I}})$, where μ_0 is the Bohr magneton, and g_L , g_S , and g_I are the orbital, electronic, and nuclear spin g values, respectively. The deviations of the magnetic field from its mean value, and the Stark and microwave fields, as well as the weak perturbation, are included in the residual perturbation Hamiltonian $V_Z(t)$. All these perturbations are small on the Rydberg scale and off-shell mixing may be neglected. The Zeeman eigenstates and eigenvalues in the $n=2$ shell are obtained as column vectors of the matrix \underline{A} and diagonal elements λ_n of the diagonal energy matrix $\underline{\Lambda}^Z = \underline{\Lambda}_r^Z - i\hbar \underline{\Gamma}^Z/2$, such that

$$\underline{H}_Z |_{n=2} \underline{A} = \underline{A} \underline{\Lambda}^Z \quad \text{and} \quad \lambda_n = E_n^Z - i\hbar \Gamma_n/2, \quad (9)$$

where $\underline{\Lambda}_r^Z$ and $\hbar \underline{\Gamma}^Z/2$ are the real and imaginary parts of $\underline{\Lambda}^Z$, respectively, and the Γ_n are the level widths. In this interaction representation a state vector \vec{v} will propagate according to

$$i\hbar \dot{\vec{v}}(t) = [V_Z(t) - i\hbar \underline{\Gamma}_Z/2] \vec{v}(t), \quad (10)$$

where the perturbation matrix $\underline{V}_Z(t)$ is obtained from the restriction of the perturbation $V(t)$ to the $n=2$ shell with

$$\underline{V}_Z(t) = e^{i\Delta_r^Z t/\hbar} \underline{A}^{-1} V(t) |_{n=2} \underline{A} e^{-i\Delta_r^Z t/\hbar}. \quad (11)$$

While the Zeeman basis is particularly appropriate for expressing the boundary conditions in our experiment, we also find it convenient to transform away the static part of the Stark interaction resulting from the presence of the applied electric field, motional or otherwise. This permits us to isolate the residual variations of the static field, which are associated with the fringing fields, in the time-dependent integration. The Stark-perturbed basis is then defined, in analogy with the Zeeman basis, by diagonalizing the Stark Hamiltonian $H_S = H_Z + e \vec{\mathbf{E}}_a \cdot \vec{r}$,

$$\underline{H}_S |_{n=2} \underline{Q} = \underline{Q} \underline{\Delta}_S, \quad (12)$$

in the $n=2$ shell. Here \vec{E}_a is the mean value of the applied electric field through the transition region. The Stark-perturbed states are the column vectors of the matrix \underline{Q} , and the Stark energies E_n^S and decay rates $-\hbar\Gamma_n^S/2$ are the real and imaginary part of the diagonal energy matrix $\underline{\Delta}_S$. Since the diagonalization (12) is performed exactly, level shifts¹⁶ and phase mixings¹⁷ are absorbed in this interaction representation. The use of this interaction picture is particularly useful when the electric field strength remains below the critical value,^{16,18} so that the perturbed states, $|\alpha\rangle_S$ and $|\beta\rangle_S$, can be identified. The time evolution of a state vector $u(t)$ is described by

$$i\hbar\dot{\vec{u}}(t) = [\underline{V}_S(t) - i\hbar\underline{\Gamma}_S/2]\vec{u}(t), \quad (13)$$

where the perturbation matrix

$$\underline{V}_S(t) = e^{i\Delta_r^S t/\hbar} \underline{Q}^{-1} [\underline{V}_Z(t) - e\vec{E}_a \cdot \vec{r}] |_{n=2} \underline{Q} e^{-i\Delta_r^S t/\hbar} \quad (14)$$

and now contains only the variation of the Zeeman and Stark interactions from their mean values, in addition to the microwave state and weak perturbations. The Hamiltonian H_S is not Hermitian so that, in general, the left and right eigenvectors of H_S are not Hermitian conjugates and $\underline{Q}^{-1} \neq \underline{Q}^\dagger$. It is, however, straightforward to show that with proper normalization, left ($\langle \tilde{i} |$) and right ($| \tilde{j} \rangle$) eigenvectors of H_S satisfy the orthogonality relation $\langle \tilde{i} | \tilde{j} \rangle = \delta_{ij}$.^{19,20} For our experimental configuration, where most of the external fields are spatially confined, one can define a transit time τ such that the system propagates freely in the Zeeman basis outside the interval $[0, \tau]$. The final state in the Zeeman basis, $v(\tau)$ may be obtained from the initial state $v(0)$ with

$$\vec{v}(\tau) = \underline{Q} e^{-i\Delta_r^S \tau/\hbar} \underline{U}_S(\tau, 0) \underline{Q}^{-1} \vec{v}(0), \quad (15)$$

where $\underline{U}_S(\tau, 0)$ is the time-evolution operator in the Stark-perturbed basis. To obtain $\underline{U}_S(\tau, 0)$ several further simplifications may be performed. The basis set may be limited to the $|\alpha\rangle_S$, $|\beta\rangle_S$, and $|e\rangle_S$ states, since, for example, the Stark-perturbed $2P_{3/2}$ states are coupled to the initial $|\alpha\rangle_S$ states through the nonresonant (1600-MHz) microwave electric field. In our experiments these couplings lead to minute contributions to the final $|\beta\rangle_S$ state amplitudes.¹⁸ Similar considerations permit us to neglect couplings to the perturbed $|f\rangle_S$ states and the effects of counter-rotating waves.²¹ Finally, when dealing with the $\alpha_0 \rightarrow \beta_0$ transition, the $|\alpha_{+1}\rangle_S$ state can also be ignored.

In the Stark representation the microwave electric dipole interaction $V_\mu = \frac{1}{2} e \vec{\epsilon} \cdot \vec{r} e^{-i\omega t}$ dominates, so it is convenient to solve (13) by treating the time-dependent fluctuation of the Zeeman field $\delta H_Z(t) = \mu_0 \delta \vec{B}(t) (g_L \vec{L} + g_S \vec{S} + g_I \vec{I})$ and Stark $\delta H_S = e \delta \vec{E}(t) \cdot \vec{r}$ Hamiltonians, as well as the weak Hamiltonian H_w , as smaller perturbations.

The solution to (13) is then obtained as the sum of four contributions

$$\vec{u}(t) = \vec{u}^\mu(t) + \delta \vec{u}^Z(t) + \delta \vec{u}^S(t) + \delta \vec{u}^W(t), \quad (16)$$

$$i\hbar\dot{\vec{u}}^\mu(t) = \underline{V}_S^\mu \vec{u}^\mu(t), \quad (17)$$

$$i\hbar \begin{pmatrix} \delta \dot{\vec{u}}^Z \\ \delta \dot{\vec{u}}^S \\ \delta \dot{\vec{u}}^W \end{pmatrix} = \underline{V}_S^\mu \begin{pmatrix} \delta \vec{u}^Z \\ \delta \vec{u}^S \\ \delta \vec{u}^W \end{pmatrix} + \begin{pmatrix} \underline{V}_S^Z \\ \underline{V}_S^S \\ \underline{V}_S^W \end{pmatrix} \vec{u}^\mu. \quad (18)$$

The four amplitudes are subject to the boundary conditions

$$\begin{aligned} \vec{u}^\mu(0) &= \underline{Q}^{-1} \vec{v}(0), \\ \delta \vec{u}^Z(0) &= \delta \vec{u}^S(0) = \vec{0}, \\ \delta u_i^W(0) &= (\underline{Q}^{-1})_{ij} \frac{V_{ji}^W}{\lambda_i - \lambda_j} v_j(0). \end{aligned} \quad (19)$$

This last boundary condition accounts for the presence of the weak mixings, which introduce some parity admixtures that modify the initial Zeeman state $v(0)$.

The relevant interference contributions to the transition probability are naturally obtained in the Zeeman representation as $\vec{v}^\mu(\tau) \cdot \delta \vec{v}^{(\alpha)*}(\tau) + c.c.$, where the amplitude $\delta v^{(\alpha)}(\tau)$ induced by the perturbation (α) is obtained from $\delta \vec{u}^\alpha(t)$ with Eq. (15). Thus each interference term can be traced to a given perturbation, so that the results are easily related to a time-dependent invariant analysis. For simplicity we have not explicitly separated the various contributions to the Stark interaction (applied and motional) in the expansion (16) although it is actually done in practice. The only weakness of the above formulation is that it is not possible to relate a line-shape distortion to a given field variation since the equations of motion are integrated numerically. This shortcoming is dealt with below with a Fourier analysis of the time-dependent interactions, analogous to well-known NMR methods.

B. Analytic results for three-level problems

Before developing more powerful methods of time-dependent invariant analysis, we obtain some valuable insights into the relations between invariant analysis and line-shape theory. They appear most clearly in some approximate analytic results for three-level systems. These results give a very accurate description of the suppressed $\alpha_0 \rightarrow \beta_0$ transition. They are also adequate for the three-level calibration transitions $\alpha_{+1} \rightarrow e_{+1} \rightarrow \beta_0$ and $\alpha_0 \rightarrow e_0 \rightarrow \beta_{-1}$, provided the initial states suffer no more than about 60% depopulation.

We have seen in Sec. IV A how it was possible, after transformation to the Stark interaction picture, to restrict the basis set to the α_S , β_S , and e_S states. We assume in the remainder of this section that the dc and microwave electric field are constant throughout the interaction region. The projection of the transformation matrix \underline{Q}^{-1} relating the Zeeman and Stark bases on the α, β, e subspace may be parametrized with four complex angles $\theta_1, \theta_2, \theta_3, \theta_4$, according to

$$\begin{aligned}
\alpha_S &\simeq \alpha, \\
\beta_0^S &= \cos\theta_1 \beta_0 - \sin\theta_3 e_0 - \sin\theta_1 e_{+1} - \sin\theta_4 f_{-1}, \\
e_0^S &= \cos\theta_2 e_0 + \sin\theta_3 \beta_0, \\
e_{+1}^S &= \sin\theta_1 \beta_0 + \cos\theta_1 e_{+1},
\end{aligned} \tag{20}$$

where we have assumed that the β_0 - e_0 and β_0 - f_{-1} mixings (hyperfine suppressed) remain small. In this approximation the angles θ_3 and θ_4 may be obtained from

$$\begin{aligned}
\sin\theta_3 &\simeq \frac{\sqrt{3}ea_0 \sin\Theta (E_{\parallel} + V^W)}{E_{\beta_0} - E_{e_0} + i\hbar\Gamma/2}, \\
\sin\theta_4 &\simeq -\frac{\sqrt{6}ea_0 \sin\Theta E^+}{E_{\beta_0} - E_{f_{-1}} + i\hbar\Gamma/2}.
\end{aligned} \tag{21}$$

If, in addition, the dc field strength is small compared to the $2P$ level width Γ ,

$$\begin{aligned}
\cos\theta_1 &\simeq \cos\theta_2 \simeq 1, \\
\sin\theta_1 &\simeq -\frac{\sqrt{6}ea_0 \cos\Theta E^-}{E_{\beta_0} - E_{e_{+1}} + i\hbar\Gamma/2}.
\end{aligned} \tag{22}$$

Here Θ is the hyperfine mixing angle, E_{\parallel} and E^{\pm} are the spherical components of the electric field²² and $V^W = \langle \beta_0 | H^W | e_0 \rangle$, the weak matrix element, is given by

$$V^W = 2i\bar{V}C_{2p} \cos\Theta. \tag{23}$$

\bar{V} is a dimensional factor equal to 1.28×10^{-2} Hz.

In the Stark representation, the initial state α_S is coupled via the microwave electric field primarily to the P states (e_S), with only a weak coupling to the final state β_S . Thus we can accurately determine the amplitude $\alpha_S(t)$ by solving the two level α_S - e_S equations of motion. The amplitude $\beta_S(t)$ is then obtained by solving the equation of motion involving the coupling of α_S and β_S states in which the amplitude $\alpha_S(t)$ is treated as a known driving term. This solution is valid as long as the α_S - β_S coupling is weak compared to the α_S - e_S coupling, a condition automatically satisfied on the α_0 - β_0 transition because of the hyperfine decoupling. The complete solution for the transition probability results from transforming $\alpha_0^S(t)$, $\beta_0^S(t)$, $e_0^S(t)$, and $e_{+1}^S(t)$ into the Zeeman basis.

The microwave couplings in the Stark representation may be obtained from the associated matrix elements in the Zeeman basis with Eq. (20). For example, the microwave couplings are given for the calibration resonance by

$$R_1^S = {}_S \langle \tilde{\alpha}_{+1} | V_{\text{rf}}^S | e_{+1} \rangle_S = R_1 \cos\theta_1$$

and

$$R^S = {}_S \langle \tilde{\alpha}_{+1} | V_{\text{rf}}^S | \beta_0 \rangle_S = -R_1 \sin\theta_1, \tag{24}$$

where $R_1 = (\sqrt{3}/2)ea_0\epsilon_{\parallel} \cos\Theta$. Similarly, the microwave matrix elements for the $\alpha_0 \rightarrow e_0, e_{+1} \rightarrow \beta_0$ transition are given by

$$\begin{aligned}
R_1^S &= {}_S \langle \tilde{\alpha}_0 | V_{\text{rf}}^S | e_0 \rangle_S = R_1 \cos\theta_2, \\
R_2^S &= {}_S \langle \tilde{\alpha}_0 | V_{\text{rf}}^S | e_{+1} \rangle_S = R_2 \cos\theta_1, \\
R^S &= {}_S \langle \tilde{\alpha}_0 | V_{\text{rf}}^S | \beta_0 \rangle_S = -R_1 \sin\theta_3 - R_2^+ \sin\theta_1 - R_2^- \sin\theta_4,
\end{aligned} \tag{25}$$

where $R_2^+ = -(\sqrt{6}/2)ea_0\epsilon_{+} \sin\Theta$ and $R_2^- = (\sqrt{6}/2) \times ea_0\epsilon_{-} \cos\Theta$.

Using these definitions, the equations of motion for both transitions reduce to the same form

$$i\hbar \begin{pmatrix} \dot{\alpha}_S(t) \\ \dot{\beta}_S(t) \\ \dot{e}_S(t) \end{pmatrix} = \begin{pmatrix} 0 & R^S e^{i\Delta_{\alpha\beta}t} & R_1^S e^{i\Delta_{ae}t} \\ R^S e^{-i\Delta_{\alpha\beta}t} & -i\hbar\gamma_{\beta}/2 & 0 \\ R_1^S e^{-i\Delta_{ae}t} & 0 & -i\hbar\Gamma^S/2 \end{pmatrix} \begin{pmatrix} \alpha_S(t) \\ \beta_S(t) \\ e_S(t) \end{pmatrix} \tag{26}$$

in the rotating-wave approximation. We have used the shorthand notation $\Delta_{\alpha\beta}$ for the detuning frequency $(E_{\alpha}^S - E_{\beta}^S)/\hbar - \omega$. Similarly, γ_{β} and Γ^S denote the Stark widths of the β_S and e_S states. The quantities R^S and R_1^S may be obtained from Eqs. (21) and (25) by substituting $-e_{\mp}$ and $-E^{\mp}$ for ϵ_{\pm} and E^{\pm} . For dc and microwave Stark couplings small compared to the natural width of the P state we may neglect all exponential terms containing Γ . Using the approximate initial conditions $\alpha_S(0) \simeq 1$, $\beta_S(0) = e_S(0) \simeq 0$ we obtain

$$\begin{aligned}
\alpha_S(t) &= e^{-(i\sigma_{\alpha} + \gamma_{\alpha}/2)t}, \\
\beta_S(t) &= \frac{R^S/\hbar e^{-\gamma_{\beta}t/2}}{\omega' - i(\gamma_{\beta} - \gamma_{\alpha})/2} (e^{[-i\omega' - (\gamma_{\alpha} - \gamma_{\beta})/2]t} - 1), \\
e_S(t) &= \frac{(R_1^S/\hbar) e^{[-i(\Delta_{ae} + \sigma_{\alpha}) - \gamma_{\alpha}/2]t}}{\omega'' - i(\Gamma - 2\gamma_{\alpha})/2},
\end{aligned} \tag{27}$$

where we have adsorbed the ac Stark shift of the α state,

$$\sigma_{\alpha} - i\gamma_{\alpha}/2 = \frac{|R_1/\hbar|^2}{\Delta_{ae}^2 + \Gamma^2/4} (-\Delta_{ae} - i\Gamma/2), \tag{28}$$

in the frequency shifts ω' and ω'' ,

$$\begin{aligned}
\omega' &= \Delta_{\alpha\beta} + \sigma_{\alpha}, \\
\omega'' &= -\Delta_{ae} - 2\sigma_{\alpha},
\end{aligned} \tag{29}$$

which also contain the dc Stark shifts in the quantities Δ . One of the most distinctive features of the final-state amplitudes (27) is that they are products of a transition moment R and a line-shape factor. With the use of Eqs. (21)–(23) and (25), the transition moments may be decomposed in terms of complex (vectorlike) invariants as well

as the scalar invariants which were encountered in Sec. III. For example, we find

$$R_1^S = j_1^{\parallel}(\vec{\epsilon} \cdot \hat{B}), \quad R_2^S = j_2^{\perp} \epsilon_+,$$

and

$$R^S = j^{\parallel}(\vec{\epsilon} \cdot \hat{B}) + g^{\parallel}(\vec{\epsilon} \cdot \hat{B})(\vec{E} \cdot \hat{B}) + g^{\perp}(\vec{\epsilon} \cdot \vec{E})_{\perp} + h^{\perp}(\vec{\epsilon} \cdot \vec{E} \times \hat{B}), \quad (30)$$

where $(\vec{\epsilon} \cdot \vec{E})_{\perp}$ refers to the scalar product of the projections of $\vec{\epsilon}$ and \vec{E} in the plane perpendicular to \hat{B} . In Eq. (30), the invariant coefficients j , g , and h carry the phase information which determines the structure of the interference term in the transition probabilities. This decomposition expresses only the rotational symmetries between the initial and final states since transition amplitudes are not direct observables. The final β -state amplitude in the Zeeman basis may be found with the transformation

$$\beta(t) = \beta_S(t) \cos\theta_1 - \sin\theta_1 e_S(t) \quad (31)$$

for three-level resonances, and

$$\beta(t) = \beta_S(t) \cos\theta_1 \quad (32)$$

for the $\alpha_0 \rightarrow \beta_0$ transition. In the latter case, the transition probability reduces to

$$|\beta(t)|^2 = |R^S/\hbar|^2 |\cos\theta_1|^2 \times \left[\frac{e^{-\gamma\alpha t} + e^{-\gamma\beta t} - 2e^{-(\gamma\alpha + \gamma\beta)t/2} \cos(\omega' t)}{\omega'^2 + (\gamma\alpha - \gamma\beta)^2/4} \right]. \quad (33)$$

This analytic expression accounts for the microwave and Stark broadening and shifts of the initial (α) and final (β) states and the finite transit time which induces Fourier components in the wings of the resonance. Using the results obtained in Eqs. (31) and (32), we find that the invariant decomposition of $|R^S|^2$ can be reduced to the forms of Eqs. (3) and (5), where $G_3 = G_4 = J_1 = J_3 = J_4 = 0$.

Thus, we find that for uniform field distributions, the transition line shape factors from the invariant decomposition, a result which justifies the analysis of systematic effects carried out in Sec. III. For weak microwave fields, it is also legitimate to use (33) for the line shape of the three-level resonances, since the electric field switches on and off slowly and the β -state amplitude follows adiabatically from the Stark to Zeeman basis. Since the line shapes are identical, time-dependent effects, such as the frequency modulation induced by Zeeman field inhomogeneities, will have the same effects on the $\alpha_0\text{-}\beta_0$ and calibration transitions. To analyze the effect of time-dependent field distributions it is necessary to obtain the complete structure of the time-evolution operator $\underline{U}_S(0, \tau)$ in the Stark basis. We may readily identify the expressions obtained for $\alpha_S(\tau)$, $\beta_S(\tau)$, and $e_S(\tau)$ in Eq. (27) with $U_S^{\alpha\alpha}$, $U_S^{\beta\alpha}$, and $U_S^{\alpha\alpha}$. Similarly, we may solve the system (26) with the boundary conditions $\beta_S(0) \simeq 1$ and $e_S(0) \simeq 1$ to obtain

$$\begin{aligned} U_S^{\beta\beta} &\simeq e^{-\gamma\beta t/2}, \\ U_S^{ee} &\simeq \left[\frac{R_1^S/\hbar}{\omega'' - i(\Gamma - 2\gamma\alpha)/2} \right]^2 e^{(-i\sigma\alpha - \gamma\alpha/2)t}, \\ U_S^{\alpha\beta} &= \frac{R^{S'}}{\hbar} e^{-\gamma\alpha t/2} \left[\frac{e^{[i\omega' - (\gamma\beta - \gamma\alpha)/2]t} - 1}{-\omega' - i(\gamma\beta - \gamma\alpha)/2} \right], \\ U_S^{e\beta} &\simeq 0, \\ U_S^{\alpha e} &= \frac{R_1^S}{\hbar} \frac{e^{[i(\Delta_{ae} - \sigma\alpha) - \gamma\alpha/2]t}}{\omega'' - i(\Gamma - 2\gamma\alpha)/2}, \\ U_S^{\beta e} &\simeq 0. \end{aligned} \quad (34)$$

This time-evolution operator describes quite accurately the α_0, e_0, β_0 three-level system. A matrix element U_{ij} can be factorized as $R^{ij}L^{ij}$ where R^{ij} is a transition moment and L^{ij} a line-shape factor. This result will be very convenient in analyzing time-dependent effects as well as performing the phase-space average of the transition probability in inhomogeneous fields, as we now demonstrate.

C. Time-dependent invariant analysis

Equation (10) may be rewritten in a more physical form by constructing from a generic perturbation $V_S(t)$ which vanishes outside the interaction region $[0, \tau]$, a periodic function of period τ which coincides with V_S inside the interaction region

$$V_S(t) = h(t) \sum_n V_n e^{2i\pi n t/\tau}, \quad (35)$$

where $h(t) = 1$ in the interval $[0, \tau]$ and $h(t) = 0$ otherwise. If the generic perturbation $V_S(t)$ is to describe the spatial variation of a rf field from its mean value an overall factor $e^{-i\omega t}$ is to be included. The amplitude $\delta\vec{u}(t)$ induced by the perturbation $V_S(t)$ may be obtained as a particular solution of the differential equation

$$i\hbar\delta\ddot{\vec{u}}(t) = \underline{V}_S^{\mu} \delta\vec{u}(t) + h(t) \sum_n V_n e^{2i\pi n t/\tau} \vec{u}_{\alpha}^{\mu}(t, 0), \quad (36)$$

where \underline{V}_S^{μ} is a uniform microwave perturbation and $\vec{u}_{\alpha}^{\mu}(t, 0)$ the corresponding solution to Eq. (17) for which the system is in the α state at $t = 0$. We seek the particular solution to Eq. (36) in the form of $\underline{U}_S(t, 0)\vec{g}(t)$, where \underline{U}_S is the time-evolution operator associated with Eq. (17). Approximate expressions for \vec{u}_{α}^{μ} and \underline{U}_S were given in Eqs. (27) and (34). $\vec{g}(t)$ is a column vector which satisfies the differential relation

$$i\hbar\underline{U}_S(0, t)\vec{g}(t) = h(t) \sum_n \underline{V}_n e^{2i\pi n t/\tau} \vec{u}_{\alpha}^{\mu}(t, 0) \quad (37)$$

which may be readily integrated in the interval $[0, \tau]$. It follows that the particular solution to Eq. (36) is

$$\delta\vec{u}(\tau) = \int_0^{\tau} \underline{U}_S(\tau, t) \left[\sum_n \underline{V}_n e^{2i\pi n t/\tau} \right] \vec{u}_{\alpha}^{\mu}(t, 0). \quad (38)$$

Denoting the projection of $\underline{U}_S(\tau, t)$ on the final β state by $\vec{u}_{\beta}^{\mu}(\tau, t)$, the final amplitude induced by the perturbation

\underline{V}_S may be expressed as an inner product,

$$\delta\beta(t) = \sum_n \int_0^\tau \bar{u}_\beta^\mu(\tau, t) \underline{V}^n \bar{u}_\alpha^\mu(t, 0) e^{2in\pi t/\tau} dt. \quad (39)$$

The analytic results obtained in Sec. IV B have shown that only two elements, $U_{\beta\beta}$ and $U_{\beta\alpha}$, of \bar{u}_β^μ are sizable and that $U_{\beta\beta} \gg U_{\beta\alpha}$. Separating the transition moment R_{ij} from the line-shape factor L_{ij} in U_{ij} , we define the amplitudes

$$a_l^n(\omega, \tau) = \int_0^\tau L_{\beta\beta}(\tau, t) L_{l\alpha}(t, 0) e^{2in\pi t/\tau} dt \\ \simeq e^{-\gamma\beta\tau/2} \int_0^\tau L_{l\alpha}(t, 0) e^{(2in\pi/\tau + \gamma\beta/2)t} dt \quad (40)$$

and

$$b_l^n(\omega, \tau) = \int_0^\tau L_{\beta\alpha}(\tau, t) L_{l\alpha}(t, 0) e^{2in\pi t/\tau} dt,$$

such that the transition amplitude $\delta\beta(t)$ can be written as

$$\delta\beta(t) = \sum_{l,m} V_{\beta l}^n [R_{l\alpha} a_l^n(\omega, \tau) + R_{\beta\alpha} b_l^n(\omega, \tau)]. \quad (41)$$

We have shown in Sec. III that all the transition moments R could be written in terms of invariants. This result is a consequence of rotational symmetry and holds also for the transition matrix elements $V_{\beta l}^n$ which, for any dipolar interaction, will be constructed from the external field Fourier harmonics $\vec{\sigma}^n$ and the electric and magnetic fields which determine the Stark mixings. Thus the scalar terms which may appear in $V_{\beta l}^n$ are $\vec{\sigma}^n \cdot \hat{B}$, $(\vec{\sigma}^n \cdot \vec{E})_\perp$, and $(\vec{\sigma}^n \cdot \vec{E} \times \vec{B})$, whereas the possible complex invariants are $\sigma^{n\pm}$, and $(\vec{\sigma}^n \cdot \vec{B})E^\pm$. Since we discuss a transition which does not change $m_f(\alpha_0 \rightarrow \beta_0)$ the invariants which appear in the final amplitude $\delta\beta(t)$ are real. This requires the contraction of the complex invariants which appear in $V_{\beta l}$ with the ones of $R_{l\alpha}$.

Because of their complex structure, any invariant pair (σ^- and ϵ_+ , for example) which arises from $V_{\beta l}^n$ and $R_{l\alpha}$, respectively, leads, after separation of real and imaginary parts, to two scalar invariants, $(\vec{\epsilon} \cdot \vec{\sigma})_\perp$ and $(\vec{\epsilon} \cdot \vec{\sigma} \times \vec{B})$. Thus the construction of the invariant decomposition of the sum $\sum_l V_{\beta l} R_{l\alpha}$ is quite straightforward and can, to lowest order, be reduced to $(\vec{\epsilon} \cdot \hat{B})(\vec{\sigma} \cdot \vec{B})$, $(\vec{\epsilon} \cdot \vec{\sigma})_\perp$, and $[\vec{\epsilon} \cdot (\vec{\sigma} \times \hat{B})]$. Since $\delta\beta(t)$ is small compared to $\beta(t)$ only the invariant structure of the interference term needs to be considered in the transition probability. With each line-

shape factor

$$\text{Re}[L_{\alpha\beta}(\omega, \tau) a^n(\omega, \tau)], \quad \text{Im}[L_{\alpha\beta}(\omega, \tau) a^n(\omega, \tau)], \quad \text{etc.},$$

will be associated several scalar invariants which are readily obtained from the possible products of any of the three invariants $(\vec{\epsilon} \cdot \vec{E})(\vec{\epsilon} \cdot \hat{B})$, $(\vec{\epsilon} \cdot \vec{E})_\perp$, and $(\vec{\epsilon} \cdot \vec{E} \times \hat{B})$ which enter the amplitude $\beta_0(t)$ and the invariants which enter the sum $\sum_l V_{\beta l} R_{l\alpha}$. We conclude that the invariants which arise in time-dependent situations may be classified as generated by "static fields," which are the respective harmonic components of the microwave field, the magnetic field, or, of most importance, the electric field. Each of the line-shape factors will induce some characteristic distortion of the transition line shape which will be analyzed in detail in Sec. V. Postponing all the complications which are associated with the relative phase variation of $\beta(\omega, \tau)$ and $\delta\beta(\omega, \tau)$ across the line, it is quite straightforward using the analytic expressions for $U(\omega, \tau)$ given in (34) to show that the amplitude $a^n(\omega, \tau)$ and $b^n(\omega, \tau)$ will have their resonance centers shifted by a frequency of the order of n/τ with respect to the α_0 - β_0 energy difference. The interference term between these ghost amplitudes $a^n(\omega, \tau)$ and $b^n(\omega, \tau)$ and the main amplitude $\beta_0(\omega, \tau)$ will thus be appreciable only if n is small, i.e., they have a sizeable overlap. For this reason, the invariant analysis for time-dependent fields which is illustrated in Table III includes only the first harmonic in the field variations. We have, for purposes of this discussion, made the simplifying assumption that \vec{E} and \vec{B} are orthogonal everywhere, i.e., $\vec{E}^0 \cdot \vec{B}^0 = \vec{E}^1 \cdot \vec{B}^0 = \vec{E}^0 \cdot \vec{B}^1 = 0$, which is correct for a motional electric field.

Some general observations are appropriate here. First, as the time-dependent invariant decomposition involves complex Fourier harmonics, each term of Table III will correspond to two distinct invariants. These are induced by variations of the fields which are, respectively, odd and even with respect to the center of symmetry of the interaction region. These symmetry properties will be shown with specific examples to induce even and odd distortions of the resonance line shapes. Thus a large fraction of the interference terms will make no contribution to an asymmetry if it is integrated over the α_0 - β_0 resonance line shape. This realizes a significant simplification of the data analysis.

TABLE III. Time-dependent invariant decomposition for the $\alpha_0 \rightarrow \beta_0$ transition rate.

Static	$G_1(\vec{\epsilon}^0 \times \hat{B}^0)^2 (\vec{E}^0 \times \hat{B}^0)^2 + G_2(\vec{\epsilon}^0 \times \hat{B}^0 \cdot \vec{E}^0 \times \hat{B}^0)^2 + G_8(\vec{\epsilon}^0 \times \hat{B}^0 \cdot \vec{E}^0 \times \hat{B}^0)(\vec{\epsilon}^0 \times \vec{E}^0 \cdot \hat{B}^0)$
Microwave electric field variation	$R_1(\vec{\epsilon}^0 \times \hat{B}^0 \cdot \vec{\epsilon}^1 \times \hat{B}^0)(\vec{E}^0 \times \hat{B}^0)^2 + R_2(\vec{\epsilon}^0 \times \hat{B}^0 \cdot \vec{E}^0 \times \hat{B}^0)(\vec{\epsilon}^0 \times \hat{B}^0 \cdot \vec{E}^0 \times \hat{B}^0) \\ + R_3(\vec{\epsilon}^0 \times \vec{\epsilon}^1 \cdot \hat{B}^0)(\vec{E}^0 \times \hat{B}^0)^2 + R_4(\vec{\epsilon}^1 \times \hat{B}^0 \cdot \vec{E}^0 \times \hat{B}^0)(\vec{\epsilon}^0 \times \vec{E}^0 \cdot \hat{B}^0) \\ + R_5(\vec{\epsilon}^0 \times \hat{B}^0 \cdot \vec{E}^0 \times \hat{B}^0)(\vec{\epsilon}^1 \times \vec{E}^0 \cdot \hat{B}^0) + R_6(\vec{\epsilon}^0 \times \vec{E}^0 \cdot \hat{B}^0)(\vec{\epsilon}^0 \times \vec{E}^0 \cdot \hat{B}^0)$
dc magnetic	$M_1(\vec{\epsilon}^0 \times \hat{B}^0)^2 (\vec{E}^0 \times \hat{B}^0)^2 (\hat{B}^1 \cdot \hat{B}^0) + M_2(\vec{\epsilon}^0 \times \hat{B}^0 \cdot \vec{E}^0 \times \hat{B}^0)(\vec{\epsilon}^0 \times \vec{E}^0 \cdot \hat{B}^0)(\hat{B}^1 \cdot \hat{B}^0) \\ + M_3(\vec{\epsilon}^0 \times \hat{B}^0 \cdot \vec{E}^0 \times \hat{B}^0)^2 (\hat{B}^1 \cdot \hat{B}^0)$
dc electric field variation	$D_1(\vec{\epsilon}^0 \times \hat{B}^0)^2 (\vec{E}^0 \times \hat{B}^0) \cdot (\vec{E}^1 \cdot \hat{B}^0) + D_2(\vec{\epsilon}^0 \times \hat{B}^0)^2 (\vec{E}^0 \times \vec{E}^1 \cdot \hat{B}^0) \\ + D_3(\vec{\epsilon}^0 \times \hat{B}^0 \cdot \vec{E}^0 \times \hat{B}^0)(\vec{\epsilon}^0 \times \hat{B}^0 \cdot \vec{E}^1 \times \hat{B}^0) + D_4(\vec{\epsilon}^0 \times \hat{B}^0 \cdot \vec{E}^0 \times \hat{B}^0)(\hat{B}^0)(\vec{\epsilon}^0 \times \vec{E}^1 \cdot \hat{B}^0) \\ + D_5(\vec{\epsilon}^0 \times \hat{B}^0 \cdot \vec{E}^1 \times \hat{B}^0)(\vec{\epsilon}^0 \times \hat{B}^0) + D_6(\vec{\epsilon}^0 \times \vec{E}^0 \cdot \hat{B}^0)(\vec{\epsilon}^0 \times \vec{E}^1 \cdot \hat{B}^0)$

V. APPLICATION OF THE TIME-DEPENDENT ANALYSIS

We focus here on the time-dependent effects which were found to be important in the experiment. Among them are the effects of magnetic field inhomogeneities and the dependence of the Zeeman energies and motional electric field on the geometrical alignments for an atomic beam of finite size and divergence. It is shown, in particular, that to a specific misalignment of the atomic beam (a tilt, or an offset with respect to the symmetry center of the interaction region), corresponds to a specific line shape for the asymmetry as the direction of the electric field is reversed. Moreover, we find that if the beam axis passes through the symmetry axis of the interaction region such asymmetries vanish. Finally, if the alignment is imperfect, then some residual asymmetries will vanish identically over the line shape if the electric and microwave field strengths have been adjusted so that the ac and dc Stark widths γ_a and γ_b , respectively, for the initial and final states are equal. We found that the agreement between the observed and predicted line shapes for the asymmetries as well as the overall dependences on field strengths to be remarkable. We believe that this analysis goes beyond PNC experiments and should find other applications in atomic physics.

A. Effects of magnetic field inhomogeneities

There are two contributions to the variation of the magnetic field strength $|\vec{B}|$, the nonuniformity of the Zeeman field δB_0 , and the component of the transverse field \vec{B}_T along B_0 :

$$\delta B = \delta B_0 + \vec{B}_T \cdot \hat{B}_0. \quad (42)$$

$$|\beta(\omega', \tau)|^2 = \frac{e^{-(\gamma_a + \gamma_b)\tau/2}}{\hbar^2} |\cos\theta_1|^2 \left| \int_{-\tau/2}^{\tau/2} R_S(t) e^{-i\delta\Omega(t) + (\gamma_b - \gamma_a)t/2} e^{-i\omega't} dt \right|^2, \quad (44)$$

where ω' is now taken to be constant. The transition amplitude is proportional to the Fourier transform of an effective field distribution

$$R_S(t) e^{-i\delta\Omega(t) + (\gamma_b - \gamma_a)t/2}. \quad (45)$$

If field inhomogeneities are absent, $\delta\Omega(t)=0$, this effective field distribution has a constant phase, and the line shape must be symmetric,

$$|\beta(\omega', \tau)|^2 = |\beta(-\omega', \tau)|^2.$$

This symmetry no longer holds when the magnetic field varies, and line-shape asymmetries can be observed. The magnetic field generated by the motional field coils is significant over approximately twice the length of the interaction region. We can therefore expand the phase factor $e^{i\delta\Omega(t)}$ in a Fourier series of period 2τ ,

The measured values of δB_0 over the interaction volume were rather small ($\delta B_0/B_0 \sim 10^{-4}$) and did not introduce serious problems. Of more concern was the second term which, because of the finite size of the coils, introduced important phase variations at both ends of the transition region unless the beam axis was very accurately aligned in the symmetry plane of the coils. If the beam is parallel to this symmetry plane, $\vec{B}_T \cdot \hat{B}_0$ is an odd function with respect to the center of the interaction region. If the beam passes through the symmetry center at an angle with respect to the symmetry plane, $\vec{B}_T \cdot B_0$ will be even. Because of these important symmetry properties, we choose the origin of time at the center of the interaction region. The magnetic field inhomogeneities introduce relatively slow phase variations between the different Stark amplitudes and they are more easily accounted for by applying directly the adiabatic approximation for the final-state amplitude $\beta'_S(t)$ than by the semiperturbative approach developed in Sec. IV C. This leads, for weak fields and with the approximate boundary condition $\alpha_S \simeq 1$, to a final β_S -state amplitude

$$\beta_S(\omega', \tau) = \frac{e^{-(\gamma_a + \gamma_b)\tau/4 - i\omega'\tau/2}}{i\hbar} \times \int_{-\tau/2}^{\tau/2} R_S(t) e^{(\gamma_b - \gamma_a)t/2 - i\omega't} dt. \quad (43)$$

The variations of the dc and microwave electric fields are small in the interaction region, and the microwave field drops off rapidly in the endcaps of the cavity. Thus the ac and dc Stark widths, γ_a and γ_b , are almost constant in the transition region $[-\tau/2, \tau/2]$. The field inhomogeneities induce, through the variation in ω' , a time-dependent phase factor $e^{i\delta\Omega(t)}$ such that the final β -state population becomes

$$e^{-i\delta\Omega(t)} = \sum_{n=-\infty}^{+\infty} c_n e^{in\pi t/\tau}. \quad (46)$$

When the path of an atom is offset with respect to the symmetry plane of the motional field coils, $\delta\Omega(t)$ is even with respect to $t=0$ and the Fourier expansion simplifies to

$$e^{-i\delta\Omega(t)} = \sum_{n=0}^{\infty} A_n \cos(n\pi t/\tau), \quad (47)$$

where the expansion coefficients A_n are complex. Similarly, when the atom trajectory is tilted with respect to the symmetry plane, $\delta\Omega(t)$ is odd, and

$$e^{-i\delta\Omega(t)} = \sum_{n=0}^{\infty} [A_n \cos(n\pi t/\tau) + iB_n \sin(n\pi t/\tau)]. \quad (48)$$

Here the coefficients A_n and B_n are real. The Fourier coefficients c_n can be calculated from the measured field

distributions, and the final-state amplitude is found by summing the contributions of the Fourier harmonics,

$$\beta_n^S(\omega, t) = \frac{e^{-(\gamma_\alpha + \gamma_\beta)\tau/4 - i\omega'\tau/2}}{i\hbar} \times \int_{-\tau/2}^{\tau/2} R^S(t) e^{(\gamma_\beta - \gamma_\alpha)t/2 - i(\omega' - n\pi/\tau)t} dt, \quad (49)$$

and can be obtained in closed form if R^S is taken to be constant through the interaction region,

$$\beta_n^S(\omega, \tau) = \frac{R^S e^{-i\omega'\tau/2} i^n e^{-(\gamma_\alpha + i\omega')\tau/2} - i^{-n} e^{-(\gamma_\beta - i\omega')\tau/2}}{\hbar (\omega' - n\pi/\tau) + i(\gamma_\beta - \gamma_\alpha)/2}. \quad (50)$$

As previously noted, this amplitude is resonant at $\omega' = n\pi/\tau$. To proceed further we exploit the different symmetries of $\delta\Omega(t)$ when the beam is offset or tilted with respect to the symmetry plane of the coils. In the first instance we separate the main amplitude ($n=0$) from the ghost amplitude,

$$\delta\beta_S = \frac{1}{2} \sum_{n=1}^{\infty} A_n (\beta_n^S + \beta_{-n}^S), \quad (51a)$$

which will introduce distortions on the high- and low-frequency sides of the line through its interference $2\text{Re}(\beta_0^{S*} \delta\beta^S)$ with the main amplitude. If the motional electric field is reversed, the phase inhomogeneity $\delta\Omega(t)$ changes sign, and the Fourier coefficients are complex-conjugated. This leads to an interference term dependent on the direction of this field. Since the interference terms involve amplitudes resonant at $\omega'=0$ and $n\pi/\tau$, the first-order effect of this field reversal is a shift of the resonance line center, with no change in the maximum transition probability. This shift changes sign when the motional electric field is increased, as the Stark-induced width γ_β of the β state becomes larger than the α -state microwave linewidth γ_α . When the equality holds, the ghost and the main amplitudes have an imaginary relative phase and no interference may take place. The calculated magnetic-field-dependent asymmetry is shown in Fig. 5 as a func-

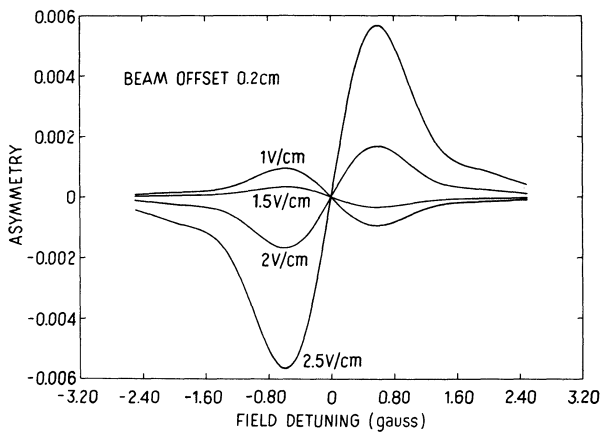


FIG. 5. Asymmetry resulting from beam offset as a function of applied electric field strength.

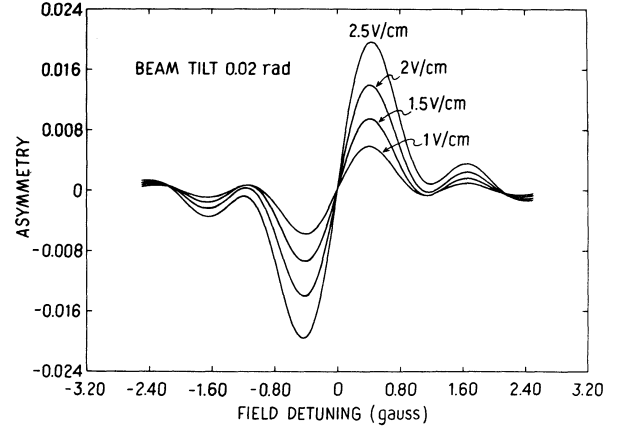


FIG. 6. Asymmetry resulting from beam tilt as a function of applied electric field strength.

tion of the applied electric field strength. When the beam is tilted with respect to the motional field coils the ghost amplitude has the structure

$$\delta\beta_S = \frac{1}{2} \sum_{n=1}^{\infty} [(A_n + B_n)\beta_n^S + (A_n - B_n)\beta_{-n}^S]. \quad (51b)$$

The reversal of the motional electric field leads to a change in sign of the coefficient B_n . The asymmetry induced by the motional field reversal is illustrated in Fig. 6. It also leads to a shift of the line center but its line shape differs qualitatively from the one observed for a beam offset, and its field dependence is monotonic. Thus a careful comparison between the observed and predicted line-shape asymmetries were of great value in aligning the beam axis in the symmetry plane of the coils. In the above analysis the finite extent and divergence of the atomic beam was not treated. In Sec. VB we show that when taken into account, the line-shape asymmetries can still be eliminated when this finite size beam is aligned in the symmetry plane of the motional field coils.

B. Phase-space average for a misaligned beam

We have shown how spurious interferences arise when an atom experiences external fields which vary in strength and direction. Along a certain symmetry axis, the fields have constant directions and systematics become negligible. With a beam of finite size and divergence, this ideal condition can only be satisfied by the atoms traveling along that axis, and the extent to which the resulting interferences average to zero when the beam axis is brought in coincidence with the field symmetry axis has to be analyzed. In our experimental configuration (Fig. 7) the "symmetry axis" is the intersection of the symmetry plane of the motional field coils with the $\vec{\epsilon} \cdot \hat{B}$ plane. To check some of the systematics another set of coils, producing a motional electric field in the y direction, was arranged so its symmetry plane would be orthogonal to the x coils and also contain the symmetry axis. An alignment procedure through which systematics were greatly reduced by moving the beam axis along the field symmetry axis using the

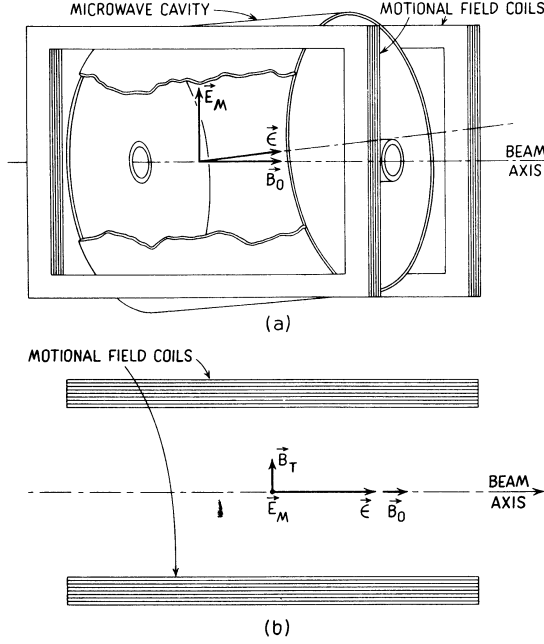


FIG. 7. Microwave cavity and coil arrangement.

calibration line $\alpha_{+1}\beta_0$ is based on the results obtained in this section.

An atom trajectory is parametrized with respect to two coordinate systems [Fig. 4(a)]. The unprimed axes comprise the laboratory system, the z axis of which coincides with the axis of the main magnetic field and the origin of which lies at the symmetry center of the microwave cavity. The primed system (beam frame) is chosen such that the symmetry axis¹¹ of the atomic beam and the z' axis are coincident. The origin of the beam frame with respect to the laboratory frame is $(x_0, y_0, 0)$. The rotational transformation is parametrized with the angles λ and χ .¹² The offset coordinates of a beam atom from $z=0$ and $z'=0$ are denoted by (μ_0, ν_0) and (μ'_0, ν'_0) , respectively. The angle between the atom's velocity and the symmetry axis of the atomic beam is Φ . We first consider the case of a nondiverging atomic beam ($\Phi=0$) for which the time-dependent coordinates of an atom are $(\mu'_0, \nu'_0 lt/\tau)$ in the beam frame, and $(\mu'_0 \cos\lambda - \nu'_0 \sin\lambda + (lt/\tau) \times \sin\lambda \sin\chi, \mu'_0 \sin\lambda + \nu'_0 \cos\lambda - (lt/\tau) \cos\lambda \sin\chi, lt/\tau)$ in

the laboratory frame, where l is the length of the microwave cavity. In the final amplitude (43), the matrix element

$$R_S(t) = {}_S \langle \beta_0 | e^{\vec{r} \cdot \vec{\epsilon}} | \alpha_0 \rangle_S \propto \langle \beta_0 | r^- E_M^+ | e_{+1} \rangle \propto E_M^x + iE_M^y,$$

where \vec{E}_M is the applied motional electric field with components $(-(v/c)B'_y \hat{x}', (v/c)B'_x \hat{y}', 0)$, and v is the speed of the atom.²² The transverse magnetic field components in the beam frame are

$$B'_x = B_T^x \cos\lambda + B_T^y \sin\lambda, \quad (52)$$

$$B'_y = -B_T^x \sin\lambda + B_T^y \cos\lambda + (B_0 + B_{Tz}^x + B_{Tz}^y) \sin\chi,$$

where B_0 is the strength of the main magnetic field and B_{Tz}^x and B_{Tz}^y are the z components of the magnetic fields of the motional field coils oriented to produce transverse fields B_T^x and B_T^y predominantly in the x and y directions, respectively. The motional electric field experienced by an atom can then be expressed in terms of the alignment angles λ and χ , and the angle ψ of the applied transverse field \vec{B}_T with respect to the $\vec{\epsilon}-\hat{B}$ plane

$$\begin{aligned} E_M^x + iE_M^y &= \frac{v}{c} (iB_T \cos\chi e^{i\psi} - B_z \sin\chi e^{i\lambda}) \\ &= (E_M^x + iE_M^y)^0 \cos\chi \\ &\quad \times \left[1 + i \frac{B_0}{B_T} \tan\chi e^{-i(\psi-\lambda)} \right], \end{aligned} \quad (53)$$

where $B_T \simeq |\vec{B}_T|$ and $B_z \simeq B_0$ and the superscript 0 refers to the field values in the absence of misalignment. Each motional field coil introduces some z field inhomogeneities which give rise to a phase modulation $\delta\Omega(t)$ in the effective field distribution (45). In the adiabatic approximation this phase drift is given by

$$\delta\Omega(t) \simeq 2\mu_0 \int_{-\tau/2}^t \delta B'_z(t') / \hbar dt', \quad (54)$$

where $\delta B'_z(t)$ is the time-dependent variation of B'_z and μ_0 is the Bohr magneton. As discussed in Sec. VA, the phase modulation is most easily accounted for by the Fourier expansion (46), the coefficients of which are obtained from $\delta B'_z$ with

$$c_n = \frac{1}{\tau} \int_{-\tau/2}^{+\tau/2} \exp \left[-i \left(\pi n \frac{t}{\tau} + \frac{2\mu_0}{\hbar} \int_{-\tau/2}^t \delta B'_z(t') dt' \right) \right] dt. \quad (55)$$

Since δB_z varies spatially, the c_n vary across the beam cross section. We show in Appendix A how the dependence of the Fourier coefficient c_n on the atom trajectory can be separated from geometrical factors which characterize the field distribution, using only two parameters f_n and g_n , which are, respectively, associated with spatially odd and even inhomogeneities with respect to the cavity center. More precisely we find

$$c_n = \frac{2i\mu_0 B_T \tau}{\hbar l} \{ f_n [\mu_0 \cos(\psi-\lambda) + \nu_0 \sin(\psi-\lambda)] - g_n l \sin\psi \sin(\psi-\lambda) \}, \quad (56)$$

where the coefficients f_n and g_n are defined in (A4). With the use of Eq. (53) the corrections to the Stark-induced coupling $R^S(t)$ associated with the misalignments can be included and the contribution of each field harmonic to the final

β_S -state amplitude becomes

$$\beta_S^{(n)}(\omega', \tau) = \cos\chi \left[1 + i \frac{B_0}{B_T} \tan\chi e^{-i(\psi-\lambda)} \right] \frac{e^{-(\gamma_\alpha + \gamma_\beta)\tau/4 - i\omega'\tau/4}}{i\hbar} \int_{-\tau/2}^{\tau/2} R_0^S(t) \exp \left[\frac{(\gamma_\beta - \gamma_\alpha)t}{2} - i\omega't + i\pi \frac{t}{\tau} \right] dt. \quad (57)$$

Combining Eqs. (56) and (57), and separating the main amplitude (zeroth harmonic) from the ghost amplitudes (higher harmonics), we find that the parameters of the atom trajectory factor out and

$$\beta_S(\omega', \tau) = \cos\chi \left[1 + i \frac{B_0}{B_T} \tan\chi e^{-i(\psi-\lambda)} \right] \times \left[\beta_S^0(\omega', \tau) + \frac{2\mu_0 B_T \tau}{\hbar l} \{ [\mu'_0 \cos(\psi-\lambda) + \nu'_0 \sin(\psi-\lambda)] f(\omega', \tau) - l \sin\chi \sin(\psi-\lambda) g(\omega', \tau) \} \right], \quad (58)$$

where the ghost amplitudes $f(\omega', \tau)$ and $g(\omega', \tau)$, given in (A5) depend only on the shape of the field distribution and not on the beam trajectory. This is the key result which permits us to average the final-state probability $|\beta_S|^2$ over the beam to account for its finite size and divergence. Since the beam source S [Fig. 4(a)] is far from the interaction region, we neglect, in first approximation, its divergence and consider just its misalignment. Keeping only the interference term between main and ghost amplitude we obtain

$$|\beta_S|^2 = \cos^2\chi \left[1 + 2 \frac{B_0}{B_T} \tan\chi \sin(\psi-\lambda) + \left[\frac{B_0}{B_T} \tan\chi \right]^2 \right] \times \left[|\beta_S^0|^2 + \frac{\mu_0 B_T \tau}{\hbar l} \{ \text{Re}(\beta_S^0 f^*) [x_0 \cos(\psi-\lambda) + y_0 \sin(\psi-\lambda)] - \text{Re}(\beta_S^0 g^*) l \sin\chi \sin(\psi-\lambda) \} \right], \quad (59)$$

where x_0, y_0 are the offset coordinates of the beam axis at $z=0$. The overall factor accounts for the variation of the Stark-induced microwave coupling associated with the misalignment. Since the line shapes of the interference terms $\text{Re}(\beta_S^0 f^*)$ and $\text{Re}(\beta_S^0 g^*)$ associated with offset and tilts of the beam are different, a careful study of the experimental line shapes enabled us to separate the alignment variables, and rapid and precise alignments could be performed.

When beam alignment is achieved ($x_0 = y_0 = \chi = 0$), all terms linear in B_0 or B_T disappear in the averaged probability. This is, unfortunately, not true when the beam divergence is considered, and a term linear in B_0 survives. To wit, consider the simple situation where the atomic beam axis is parallel to the z axis, i.e., $\chi = 0$. Then $\mu_0 = x_0 \cos\lambda + y_0 \sin\lambda$ and $\nu'_0 = -x_0 \sin\lambda + y_0 \cos\lambda$. Assuming a point beam source of maximum divergence Φ_0 (Fig. 4), the final-state probability is found by integrating over the beam cross section,

$$|\beta_S|^2 = \left[1 + \frac{1}{2} \left[\frac{B_0}{B_T} \right]^2 \Phi_0 \right] \left[|\beta_S^0|^2 + \frac{4\mu_0 B_T \tau}{\hbar l} (x_0 \cos\psi + y_0 \sin\psi) \text{Re}(\beta_S^0 f^*) - \frac{8\mu_0 B_0 \tau}{3\hbar} \Phi_0 \text{Re}(\beta_S^0 g^*) \right]. \quad (60)$$

The last term, linear in B_0 , is a systematic effect which can only be interpreted in the context of the phase-space average carried out here. It is a concern, when small applied fields are used, since the natural beam divergence contributes significantly to the Stark-induced transition rate. Fortunately, if the initial- and final-state widths, γ_α and γ_β , are equal, we find, using (50) and (A6), that $\text{Re}(\beta_S^0 g^*)$ vanishes. This result may be interpreted using the effective field distribution (45), which is constant in modulus when $\gamma_\alpha = \gamma_\beta$. In this instance, the phase modulation through the cavity averages, and the effect of field inhomogeneities become less severe. This result was observed experimentally and allowed us to set the rf field strength such that $\gamma_\alpha = \gamma_\beta$ when taking data.

The analysis carried out here has been extended¹⁸ to include all the effects associated with the variation of the matrix element R_S through the interaction region. The effects we have considered are the variation of the direction of the resultant magnetic field through the interaction region, localized stray fields, and fringing rf fields at the ends of the transition region. Only the last effect is of

some relevance to our experimental work and is briefly outlined in Appendix B. The conclusion of the analysis is that many time-dependent effects associated with inhomogeneous field distributions are suppressed when the effective field distribution (45) has a constant value through the interaction region (i.e., $\gamma_\alpha = \gamma_\beta$). The variations of $R_S(t)$ are then efficiently averaged along the beam path, and the systematic effects are efficiently suppressed. We firmly emphasize the advantage that a slow hydrogen beam experiment²³ will offer, as the systematic effects discussed above will become quite negligible.

VI. EXPERIMENTAL RESULTS

A. Apparatus and operating conditions

Figure 8 is a schematic diagram of the apparatus. The source of metastable hydrogen atoms was a Duoplasmatron ion source in combination with a cesium charge-exchange cell. A dense plasma was produced by striking a 15-A arc in a hydrogen cell at a pressure of 0.5–1 Torr

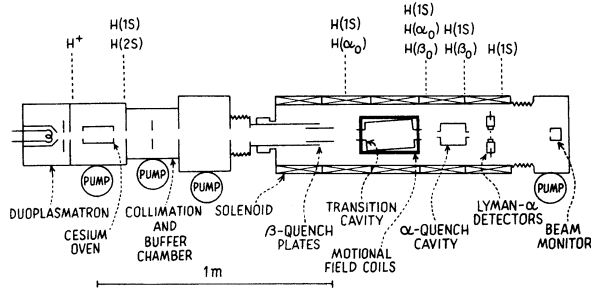


FIG. 8. Schematic diagram of the apparatus.

and with a confinement magnetic field of 1.5–2 kG. A 5-mA proton beam was extracted at an energy of 6 keV and decelerated to the beam energy of 500 eV. The protons underwent the resonant charge-exchange reaction $H^+ + Cs \rightarrow H(2S) + Cs^+$ in a 15-cm-long cesium vapor cell maintained with an oven (75°C) at the optimal target thickness of $1.4 \times 10^{14} \text{ cm}^{-2}$. This resulted in a conversion of about 15% of the incident protons to atoms in the metastable $2S$ state.

A buffer chamber maintained at a pressure below 5×10^{-8} Torr with an Orb-Ion pump followed the charge-exchange region. It contained electrostatic deflection plates to remove the protons which did not undergo charge exchange from the beam. Apertures near the entrance and exit of the buffer chamber provided a collimated atomic beam without halos. Following the exit collimator a second electrostatic deflector removed any charged particles resulting from collisions of the neutral beam with the exit collimator. The beam then entered the main vacuum chamber maintained at a pressure below 1×10^{-8} Torr with two 8-in. liquid-helium cryopumps located at each end of the main vacuum chamber. Four distinct regions were successively encountered by the atomic beam as it passes through the 1-m-long vacuum chamber: a state selector (or β -quench region), the main interaction region, a state analyzer (or α -quench region), and a detector. The Zeeman magnetic field, which extended through all regions, was produced by a solenoid constructed of five spools of high-conductivity aluminum strap. The spools fit around the aluminum cylindrical tube comprising the main vacuum chamber wall. Optimum field shaping was achieved with a larger number of turns on the outer spools and external shunt resistors for shimming. The homogeneity of the field was ± 120 mG over the central 45-cm region of the solenoid, and ± 60 mG over the main transition region, which was 13 cm long. The magnetic field was swept with a control voltage to the solenoid power supply provided by the computer. A dc relay permitted reversal of the direction of the field. Two rectangular (60×120 cm) coil pairs with mutually orthogonal axes were used to achieve precise steering of the resultant magnetic field for fine tuning of the field and beam alignment, and to cancel the component of the Earth's field transverse to the atomic beam axis.

To perform the α -state selection, we exploit the fact that approximately 25 cm inside the solenoid, the magnetic field is near the β - e level crossing. An electric field of

15 V/cm, applied with two semicylindrical plates 15 cm long, mixes the β state with the very short-lived $e(2P)$ state. The resultant Stark quenching depopulates the β beam by more than 8 orders of magnitude. To prevent leakage of the electric field into the interaction region, guard rings were placed at the end of the electrodes, and an electrostatic shield was placed in the 15-cm space which separated the β -quench region from the main transition region. The main interaction region, where the $\alpha \rightarrow \beta$ transitions were driven, contained the fields $\vec{E}, \vec{B}, \vec{\epsilon}$ in the configuration of Fig. 2. A cylindrical microwave cavity operating in the TM_{010} mode produced the constant microwave electric field $\vec{\epsilon}$ along its symmetry axis. The cavity, constructed of oxygen-free high-conductivity copper, was approximately 15 cm in diameter and 11 cm long. It comprised four radially tunable quadrants. Each of the quadrants was mounted on sapphire ball-bearing tracks and could move radially about 8 mm. These radial motions were coupled via vacuum rotary feed-throughs to the outside of the vacuum system, permitting external tuning of the resonant frequency from 1480 to 1610 MHz with little effect on the cavity Q , which is ≈ 1500 . The axis of the cavity was tilted at an angle $\approx 5^\circ$ (see Fig. 9) to the axis of the solenoid. The atomic beam entrance and exit had 3-cm-long endcaps to provide rapid cutoff of the microwave fields. A rectangular coil pair of 10 cm separation and fitted about the cavity [Fig. 7(a)], produced the magnetic field transverse to the solenoid field (y direction) to provide the motional electric field in the x direction which induces the Stark mixing of the β_0 and e_{+1} states and, together with ϵ_x , the suppressed PC α_0 - β_0 amplitude. For our beam velocity, the motional field is approximately 0.29 (V/cm)/G .

For systematic checks, a similar coil pair was arranged to produce a motional electric field in the y direction. The axes of these coils were positioned at 90° to the solenoid field to a precision of $\pm 0.1^\circ$.

After the main transition region a state analyzer was required to eliminate the α -state population which is 10^5 times that of the β state, since the α_0 - β_0 transition is high-

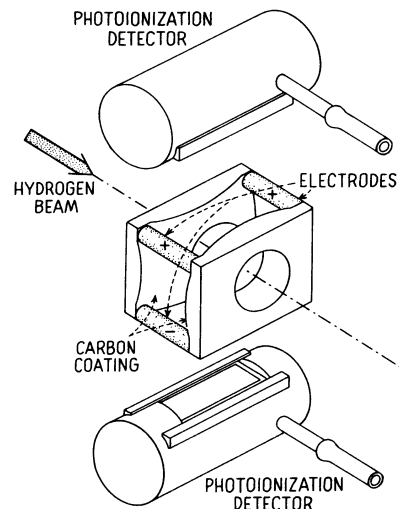


FIG. 9. Detector region.

ly suppressed. We accomplished this by driving the resonant α - f microwave electric dipole transition in a resonant cavity just prior to the β -state detection. This α -quench cavity was cylindrical, 8 cm long and 11 cm in diameter, and operated in the TM_{010} mode at a frequency of 2080 MHz with a Q of 1500. The cavity axis was perpendicular to the solenoid field.

We detected the β -state atoms by applying a localized dc electric field to quench them in the field of view of two Lyman- α photoionization detectors. This detection region was separated from the α -quench region by three light baffles to eliminate scattering of Lyman- α radiation into the photoionization detectors. As a consequence of producing the metastable hydrogen atoms by the aforementioned charge-exchange process, there is a spurious Lyman- α background in the detectors from secular cascade decay through the $2P$ states of atoms in Rydberg ($n=9-12$) states produced in the neutralization process.²⁴ With only modest electric field confinement, this background was several orders of magnitude larger than the desired signal. The discovery of its source, which produces a detector current proportional to the beam volume in the field of view of the detectors, led us to develop a highly confined quench region which improved the signal-to-background ratio to $\simeq \frac{1}{2}$. We obtained a high detector quenching efficiency with a quadrupole field configuration combined with carbon films to provide high confinement of the detector quenching electric field.²⁵ With the arrangements shown in Fig. 9 the electric field is confined to a region 6 mm in length on the beam axis. With a typical beam diameter of 1.3 mm this provides a $3\pi/4$ collection solid angle for the two detectors. The photoionization detectors are characterized by high gain (up to 10^4), large solid angle, and good quantum efficiency ($\sim 20\%$).²⁶

The detector current is amplified with a current sensitive preamplifier with sensitivity 10^7-10^9 V/A and is fed into the computer to perform a multichannel phase-sensitive detection. With these detectors, β -state beams of $0.2 \mu\text{A}$ were obtained, which corresponded to a total metastable flux greater than $10^{13} \text{ cm}^{-2} \text{ sec}^{-1}$ two meters from the source. With a 0.1-sec sampling time, the long-term stability of the beam was better than one part in 10^3 .

B. Data and discussion

To extract PNC contributions from systematic interferences (cf. Table I), we have implemented a computerized multichannel phase-sensitive detection system.²⁷ This permitted us to separate even and odd contributions to the detected transition rate as each electric or magnetic field component was reversed. A "channel" was associated with the signal of a specified symmetry under each of the field reversals. A given invariant has definite symmetries as the field components are reversed and can be associated with the corresponding channel. When the magnetic field strength was varied, the line shape of each of the resulting asymmetries, as the field directions were reversed, was recorded and compared with the predicted shape associated with systematic effects arising from beam misalignments. Since the field distributions experienced by each

atom in the beam were known and since a particular misalignment corresponded to a specific pattern of field inhomogeneities with definite symmetry with respect to the cavity center, it was possible to identify all misalignments from the observed asymmetries. It was then a simple matter to correct for these misalignments by changing the position and the orientation of the main vacuum chamber. Any small residual motional electric field resulting from a tilt of the main solenoid field with respect to the beam axis was corrected with the external transverse field coils, the resultant magnetic field direction and beam axis being brought into coincidence. Alignments of $10 \mu\text{rad}$ were achieved in this way by monitoring the residual asymmetry on the $\alpha_{+1}\beta_0$ calibration line as the electric field was reversed.

Figure 10 shows typical dependences of the $\alpha_{+1}\beta_0$ resonance line shape and residual asymmetry under reversal of the motional electric field as a function of field strength, together with the fits obtained when the residual misalignment is taken into account. We note that the asymmetry is smallest when $E_M \simeq 2 \text{ V/cm}$, the value for which $\gamma_\alpha \simeq \gamma_\beta$. This is in agreement with the prediction made in Sec. V, where we showed that when the widths of the initial and final states are equal, the phase modulation associated with beam offsets leads to no net line-shape distortion. Similarly, the unequal heights of the Fourier components in the wings of the resonance are accounted for by the residual $\pm 60\text{-mG}$ inhomogeneity of the solenoid field over the main transition region.

It is apparent from the data of Fig. 10 that the asym-

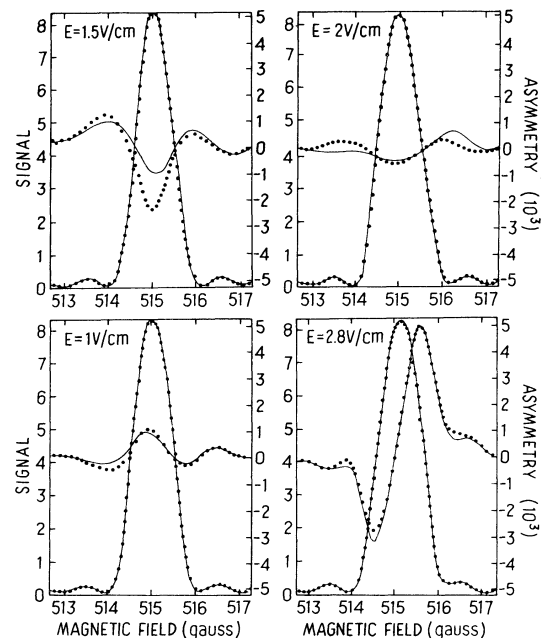


FIG. 10. Magnetic field scans of the $\alpha_{+1}\beta_0$ transition and the asymmetries under reversal of E_M (dots) for various values of E_M . Line shapes for the asymmetries are normalized to the line-center intensity, i.e., $A = [R(\omega, E_M) - R(\omega, -E_M)] / [R(\omega, E_M) + R(\omega, -E_M)]$. The line-shape fits (solid lines) were obtained with a beam tilt of 0.005 rad, a beam offset of 1.5 mm, and an imperfection of the motional field reversal of 0.06%.

metries under motional field reversal were less than 5×10^{-3} anywhere on the line for any field strength. When the electric field strengths were such that $\gamma_\alpha = \gamma_\beta$, the asymmetry was less than 2×10^{-3} . We have seen in Sec. V that there is no net asymmetry associated with misalignments when the transition probability is integrated over the entire line shape. Thus the asymmetry

$$A = \frac{\int R_+(\omega) d\omega - \int R_-(\omega) d\omega}{\int R_+(\omega) d\omega + \int R_-(\omega) d\omega} \quad (61)$$

is less sensitive to time-dependent systematic effects. This analysis resulted in an upper limit on the asymmetry under motional field reversal well below 1×10^{-3} , a limit essentially determined by the drifts in the beam direction. Figure 11 exhibits the asymmetries under reversals of \vec{E}_M and \vec{B}_0 for the strong $\alpha_{+1}\beta_0$ resonance. A shift in the resonance line center under reversal of \vec{E}_M was observed for one of the directions of the main magnetic field. This indicated a coupling between the reversals of the applied motional field and the solenoid field, and was expected, as any residual motional field-induced interference will couple these reversals. The nature of the asymmetry on the $\alpha_{+1}\beta_0$ resonance under reversal of the solenoid field is not well understood. While we knew that the reversal of the solenoid field for a fixed applied motional field was of the order of one part in 10^2 , because of the coupling of the electric and magnetic field reversals, we were not able to determine whether we could improve the asymmetry quoted for the electric field reversal alone. To take full advantage of the Zeeman reversal the magnitude of the magnetic field should be controlled with a NMR calibration. This will be available to us in future work.

A magnetic field scan in the neighborhood of the suppressed $\alpha_0 \rightarrow \beta_0$ transition yields four Stark-induced resonances, as shown in Fig. 12. The larger two of these are allowed transitions in deuterium, a result of the natural deuterium abundance of 200 ppm. The center resonance is the desired $\alpha_0 \rightarrow \beta_0$ line, which is noticeably similar to the strong $\alpha_{+1} \rightarrow \beta_0$ line. The remaining resonance is the suppressed hydrogen $\alpha_{+1} \rightarrow \beta_{-1}$ transition. This

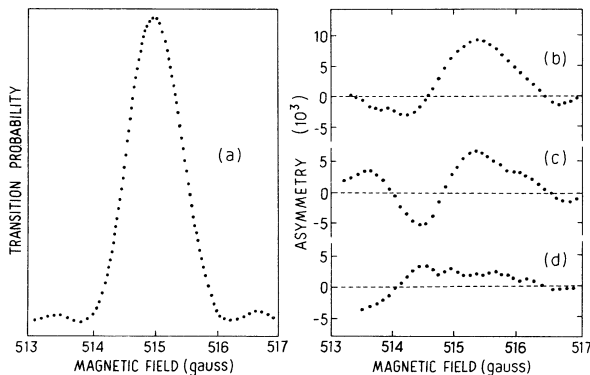


FIG. 11. Magnetic field scan of the $\alpha_{+1}\beta_0$ transition (a), and asymmetries under reversal of E_M for (b) B_0 upbeam and (c) B_0 downbeam; (d) is a combined asymmetry for reversal of \vec{E}_M and \vec{B}_0 .

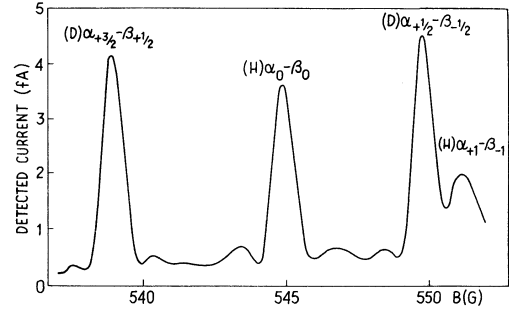


FIG. 12. Magnetic field scan in the neighborhood of the $\alpha_0\beta_0$ resonance.

transition is similar to the $\alpha_0 \rightarrow \beta_0$ resonance, but is insensitive to PNC effects. The calculated locations of the four transitions were in complete agreement with our measurements. Further, the calculated (3.8×10^{-6} of the initial α_0 population) and observed (3.5×10^{-6}) intensities agreed quite well and allowed absolute calibration of the final β_0 -state population using the deuterium resonances. The effects of field reversals on the $\alpha_0\beta_0$ transition were obtained in two different runs.²⁸ For one of these only the reversal of the direction of \vec{E}_M was employed, while for the second reversals of both \vec{E}_M and \vec{B}_0 were used.²⁹ Our best alignment was attained for the former case. The data for this situation are shown in Fig. 13, wherein the magnetic field scans across the $\alpha_0\beta_0$ transition for opposite directions of \vec{E}_M are exhibited. The upper limit on the asymmetry under this reversal is mainly statistical and is the order of 2% on a point-by-point basis. As we have noted, one gains by averaging the asymmetry over the resonance line shape to obtain the statistics of the complete scan. The upper limit which results is

$$A < 5 \times 10^{-3}. \quad (62)$$

In the second run, we obtained better statistics. The data are exhibited in Fig. 14, showing the asymmetries under reversal of \vec{E}_M for each of the two directions of \vec{B}_0 , as well as the asymmetry under combined reversals of the directions of \vec{E}_M and \vec{B}_0 . As can be seen, this asymmetry

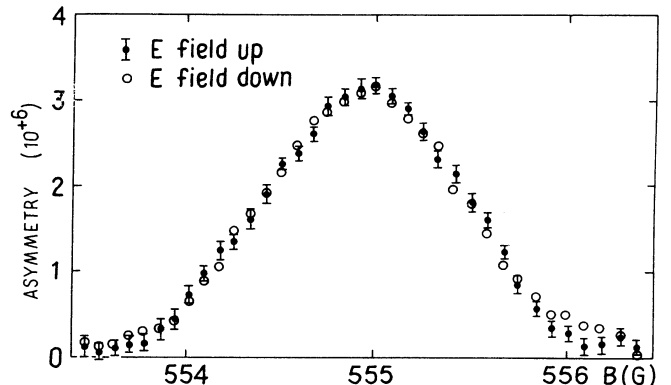


FIG. 13. Magnetic field scan of the $\alpha_0\beta_0$ transition for opposite directions of \vec{E}_M .

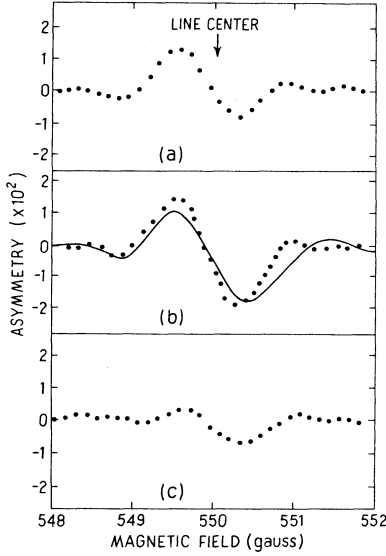


FIG. 14. Asymmetry on the $\alpha_0\text{-}\beta_0$ resonance under reversal of E_M for the two directions of \vec{B}_0 : (a) \vec{B}_0 upbeam; (b) \vec{B}_0 downbeam, (c) is the combined asymmetry for reversal of \vec{E}_M and \vec{B}_0 .

does not change sign when \vec{B}_0 is reversed, indicating that it has the characteristic of a T -odd invariant. This results, in fact, from the interference term generated by the modulation of the direction of the resultant magnetic field when the direction of \vec{B}_T is reversed (see Table I). The fit to these data for this systematic effect is the solid line of Fig. 12, which was calculated by integration of the Schrödinger equation, using the measured field distributions. The agreement is good and confirms our understanding of the line shape at the one part in 10^{-3} level. Again using the integrated asymmetry we have

$$A < 3 \times 10^{-3}. \quad (63)$$

The limits (62) and (63) on A yield for the upper limit on the $2^2S_{1/2}\text{-}2^2P_{1/2}$ PNC mixing parameter at zero magnetic field⁵

$$|\delta| < 1.5 \times 10^{-8}. \quad (64)$$

This corresponds to a limit on the weak $2^2S_{1/2}\text{-}2^2P_{1/2}$ matrix element of

$$|\langle \beta_0 | V_W | e_0 \rangle| < 16 \text{ Hz}. \quad (65)$$

In terms of the dimensionless constant for the vector electron-axial vector proton weak coupling it corresponds to

$$C_{2p} < 620. \quad (66)$$

VII. CONCLUSIONS

While we have yet to attain a sensitivity sufficient to provide significant input to unified models of electroweak interactions, we have reduced the limit on the mixing of the $2^2S_{1/2}$ and $2^2P_{1/2}$ states in atomic hydrogen by a PNC interaction by more than 4 orders of magnitude.³⁰

Of the most consequence are the developments and tests we have made which have shown that our relatively simple configuration of fields in the main interaction region, in fact, is one which will permit tests of the electroweak model at low energy at the requisite level of precision.

Finally, we have developed some elegant techniques of line-shape analysis which have allowed us to probe the structure of time-dependent interference effects in considerable detail. We can trace the phase structure of time-dependent amplitudes to the symmetry properties of field distributions, even when the beam phase space is fully included in the theory.

There are two serious problems associated with the use of Duoplasmatron-based charge-exchange sources for producing the requisite high-intensity metastable hydrogen beams for such experiments as ours. One is the cascade decay of higher-lying states of atomic hydrogen produced in charge-exchange collisions. This results in a small but significant Lyman- α background in our detectors, and, even with very stringent confinement of the detector quench region, ultimately limits the signal-to-noise ratio on the PC $\alpha_0\text{-}\beta_0$ transition to unity. The second are the considerable systematic effects arising from motional electric fields, a direct consequence of the large atom velocity. Both of these effects would disappear with the use of a slow H(2S) beam,²³ excited in such a way as to guarantee the absence of higher-lying states. As we noted above, the asymmetry we wish to observe is inversely proportional to the \sqrt{v} under optimized conditions so the slow beam will offer considerable further advantage.

ACKNOWLEDGMENTS

The authors wish to acknowledge Professor G.W.F. Drake for major help with the analysis presented here and the use of his computer program on which our numerical integration of the Schrödinger equation was based, and Professor E.S. Fry and Mr. D.D. Smith for their assistance with the experiment. The work was supported by the National Science Foundation under Grant No. PHY-79-25044 and is based on the dissertation of L.P.L. submitted in partial fulfillment for the Ph.D. degree at the University of Michigan. L.P.L. was the recipient of a Horace H. Rackham grant.

APPENDIX A

When an atom passes through a transition region where the fields are inhomogeneous in space, we show that it is possible to separate all the dependence of the $\alpha_0\text{-}\beta_0$ and $\alpha_{+1}\text{-}\beta_0$ transition line shapes on the atom trajectory from the geometrical factors associated with the field distributions. The inhomogeneities in the Zeeman field arise from the fields of either the x or the y motional field coils, which have the same dimensions but which produce different transverse fields, B_T^x and B_T^y , along the \hat{x} and \hat{y} axes, respectively. We perform a Taylor expansion of the Zeeman inhomogeneity around the symmetry axis,

$$\delta B_z(x, y, z) = \mu_0 \frac{\partial}{\partial x} \delta B_z(0, 0, z) + \nu_0 \frac{\partial}{\partial y} \delta B_z(0, 0, z). \quad (A1)$$

Since the coils have the same field distributions, it is con-

venient to define the fractional contribution to the axial field derivatives as

$$b(z) = \frac{1}{B_T^x} \frac{\partial(B_z)}{\partial x} = \frac{1}{B_T^y} \frac{\partial(\delta B_z)}{\partial y}. \quad (\text{A2})$$

Using the coordinate transformations from the laboratory frame into the atomic beam frame defined in Fig. 5 and Sec. VB, we find

$$\delta B_z'(z') = b(z') B_T [\mu'_0 \cos(\psi - \lambda) + \nu'_0 \sin(\psi - \lambda) - z' \sin\chi \sin(\psi - \lambda)]. \quad (\text{A3})$$

Assuming that the phase drift $\delta\Omega(t)$ defined in Eq. (53) remains small so we may approximate $e^{-i\delta\Omega(t)} \simeq 1 - i\delta\Omega(t)$, we obtain, for the Fourier coefficients c_n defined in (54), the closed-form expression (55). Recalling that $z' = lt/\tau$, the coefficients f_n and g_n are found to be

$$f(\omega', \tau) = \sum_{n \neq 0} f_n e^{-[i\omega' + (\gamma_\alpha + \gamma_\beta)/2]\tau/2} \int_{-\tau/2}^{\tau/2} [R_S^0(t)/\hbar] e^{[(\gamma_\beta - \gamma_\alpha)/2 - i(\omega' - n\pi/\tau)]t} dt, \quad (\text{A5})$$

and $g(\omega', \tau)$ is obtained with the same formula with f_n replaced by g_n . When the microwave electric field is assumed constant through the interaction region, $f(\omega', \tau)$ and $g(\omega', \tau)$ reduce to

$$\begin{aligned} f(\omega', \tau) &= \sum_{n (\neq 0)} f_n \beta_S^n(\omega, \tau), \\ g(\omega', \tau) &= \sum_{n (\neq 0)} g_n \beta_S^n(\omega, \tau), \end{aligned} \quad (\text{A6})$$

where the $\beta_S^n(\omega, \tau)$ are given by (49).

APPENDIX B

A brief discussion of the possible systematic effects associated with the time dependence of the microwave field is presented as an illustration of the techniques developed in Sec. V. The presence of fringing microwave fields at the entrance and the exit of the microwave cavity introduces an important time dependence of the transverse component of the microwave electric field used to drive

$$\begin{aligned} R^S &= i \frac{K}{2} \frac{v}{c} B_T \left[\epsilon_x \left[(e^{i\psi} + a e^{-i\psi}) + i \frac{B_0}{B_T} \tan\chi (e^{i\lambda} - a e^{-i\lambda}) \right] \right. \\ &\quad \left. + \epsilon_f h(t) \left[(e^{i(\psi-\lambda)} + a e^{-i(\psi-\lambda)}) + i \frac{B_0}{B_T} \tan\chi (1-a) \right] \right]. \end{aligned} \quad (\text{B3})$$

With this time dependence of the $\alpha_0\text{-}\beta_0$ transition moment, we obtain the beam averaged final-state probability using Eqs. (58) and (59):

$$f_n = -\frac{1}{l} \int_{-l/2}^{l/2} dz' e^{-in\pi z'/l} \int_{-l/2}^{z'} b(u) du \quad (\text{A4})$$

and

$$g_n = -\frac{1}{l^2} \int_{-l/2}^{l/2} dz' e^{-in\pi z'/l} \int_{-l/2}^{z'} ub(u) du.$$

The coefficients f_n and g_n describe the shape of the field inhomogeneities probed when the trajectory of the atom is, respectively, offset or tilted with respect to the symmetry axis. In these instances, the inhomogeneities are odd or even, respectively, with respect to the cavity center.

As we have seen in Sec. VB, each field harmonic will contribute to some ghost amplitudes $f(\omega', \tau)$ and $g(\omega', \tau)$, which characterize any misalignment as an offset or a tilt, but are independent of their magnitudes. Using (55) and (56) we find

the $\alpha_0\text{-}\beta_0$ transition. The endcaps of the cavity have rotational symmetry around the z axis, and the transverse component of the fringing microwave electric field ϵ_f is radial. Denoting by $h(t)$ the time-dependent variation of the fringing field along the beam axis, the transverse component of the microwave field may be parametrized by

$$\epsilon_{\pm} = \mp \frac{1}{\sqrt{2}} [\epsilon_x + \epsilon_f e^{\pm i\lambda} h(t)]. \quad (\text{B1})$$

Using the expressions (22) and (25), we find the microwave coupling between $|\alpha_0\rangle_S$ and $|\beta_0\rangle_S$ states to be

$$R^S = K(E_M^+ \epsilon_- - a E_M^- \epsilon_+), \quad (\text{B2})$$

where

$$a = \frac{E_{\beta_0} - E_{e_{+1}} + i\hbar\Gamma/2}{E_{\beta_0} - E_{f_{-1}} + i\hbar\Gamma/2},$$

and K is a proportionality factor. With the parametrization (52) of the motional field, we find

$$\begin{aligned} |\beta_S|^2 &= \left[|\beta_S^0|^2 |e^{i\psi} + a e^{-i\psi}|^2 - 2 \frac{\Phi_0}{3} \frac{\epsilon_f}{\epsilon_x} \frac{B_0}{B_T} \right. \\ &\quad \left. \times \text{Re}[i\beta_S^0 \beta_f^* (e^{i\psi} + a e^{-i\psi})(1-a^*)] \right]. \end{aligned} \quad (\text{B4})$$

Here

$$\beta_f = -ie^{-[(\gamma_\alpha + \gamma_\beta)/2 + i\omega']\tau/2} \times \int_{-\tau/2}^{\tau/2} h(t) e^{[(\gamma_\beta - \gamma_\alpha)/2 - i\omega']t} dt. \quad (\text{B5})$$

The fact that the interference term reverses sign under reversal of B_T and B_0 is of concern. However, in the parity experiment the angle ψ is zero, and the interference term is suppressed because of the imaginary relative phase of

the main amplitude and the amplitude associated with the fringing fields. Further, it vanishes for $\gamma_\alpha = \gamma_\beta$, when integrated over the line, as the spatial distribution $h(t)$ is odd with respect to the cavity center. In this analysis, higher-order effects involving the combined time dependence of the effective field distribution through the fringing microwave field, and the phase modulation induced by magnetic field inhomogeneities were ignored. This appears to be legitimate at our present level of sensitivity.

*Present address: AT&T Bell Laboratories, 600 Mountain Ave., Murray Hill, NJ 07974.

¹S. Weinberg, *Rev. Mod. Phys.* **46**, 255 (1974).

²G. Arnison *et al.*, *Phys. Lett.* **122B**, 103 (1983); **126B**, 398 (1983).

³W. J. Marciano and A. Sirlin, *Phys. Rev. D* **27**, 552 (1983).

⁴The notation is that of G. Feinberg and M. Y. Chen, *Phys. Rev. D* **10**, 190 (1974).

⁵R. R. Lewis and W. L. Williams, *Phys. Lett.* **59B**, 70 (1975); R. W. Dunford, R. R. Lewis, and W. L. Williams, *Phys. Rev. A* **18**, 2421 (1978). These are denoted, respectively, papers I and II.

⁶The role of damping in our work has been investigated experimentally. See L. P. Lévy and W. L. Williams, *Phys. Rev. Lett.* **48**, 1011 (1982). A manuscript describing this investigation in detail is in preparation.

⁷We perform the invariant decomposition in the rest frame of the atom, so its velocity v does not enter the analysis. We will include stray electric and magnetic fields at the appropriate point in the discussion.

⁸It is most convenient and provides the most physical insight to express the invariants in terms of components of the electric fields parallel and transverse to the magnetic field as in C. Dukes, H. Kwong, and R. R. Lewis (unpublished).

⁹The $M1$ amplitude for the $\alpha_0 \rightarrow \beta_0$ transition can lead to an $E1$ - $M1$ interference which changes sign under reversal of \vec{E} and \vec{B} . It is highly suppressed for our field configuration. In any case it introduces no systematic effect when the transition probability is integrated over the resonance line shape, a technique which plays a key role in our analysis.

¹⁰The field-dependent values of the invariant coefficients have been numerically calculated. The line shapes are given in Ref. 8. It is important to distinguish between two different characteristic line shapes. The magnetic-field-dependent line shapes of A_S and A_W , which describe the mixing of the $2S$ and $2P$ states, are characterized by linewidths of the order of the natural width of the $2P$ state (≈ 50 G). The microwave resonance line shapes have linewidths (< 1 G) determined by the microwave and dc Stark-induced damping of the α and β states, respectively, and by the finite transit time of $H(2S)$ atoms through the microwave cavity.

¹¹We explicitly assume that the atomic beam is cylindrically symmetric about its axis as concerns all significant characteristics. This is confirmed to high precision by our experimental results.

¹²The angles λ, χ are the Euler angles describing the transformation from the "laboratory" system, with the x - z plane defined by \vec{e} and \vec{B}_0 , to the "beam" system, wherein the polar axis is defined by the axis of cylindrical symmetry of the $H(2S)$ beam.

¹³We do not include a component of \vec{B}_T along \vec{B}_0 as this is trivi-

al to detect and correct; if $\vec{B}_T \cdot \vec{B}_0 \neq 0$, the center of the microwave resonance shifts when the directions of \vec{B}_T or \vec{B}_0 are reversed. The direction of B_T is adjusted to eliminate this shift.

¹⁴We ignore stray electric fields here as they presented no problem in the experiments carried out with applied motional fields.

¹⁵The symbol e denotes the magnitude of the charge of the electron.

¹⁶The level shifts in the vicinity of the $2S_{1/2} - 2P_{1/2}$ level crossings have been discussed in detail by W. E. Lamb, Jr., *Phys. Rev.* **85**, 259 (1952).

¹⁷As alluded to in Sec. II, the variation with magnetic field of the relative phase of the β and e states through the β - e level crossing provides a unique signature of the PNC interaction.

¹⁸L. P. Lévy, Ph.D. dissertation, University of Michigan, 1982 (available from University Microfilms, Ann Arbor).

¹⁹As we noted earlier (Ref. 6), the analysis of mixing of neutral K -mesons exploits this use of right and left eigenstates: See, e.g., S. H. Patel, Y. Tomozawa, and Y. P. Yao, *Phys. Rev.* **142**, 1041 (1965).

²⁰If the perturbation V_S is purely real, the matrix representation of H_S is symmetric but non-Hermitian: the matrix \underline{A} which transforms from the perturbed basis to the free eigenstates has the property $\underline{A}^T = \underline{A}^{-1}$.

²¹P. R. Fontana, *Atomic Radiative Processes* (Academic, New York, 1982); L. P. Lévy, Ref. 18.

²²We adopt the spherical tensor convention of A. R. Edmonds, *Angular Momentum* (Princeton University, Princeton, N.J.), pp. 168–177.

²³Production of 77-K $H(2S)$ beams has been described by K. C. Harvey, *J. Appl. Phys.* **53**, 3383 (1982). An intense beam source of slow $H(2S)$ is currently being developed in our laboratory.

²⁴This will be described by L. P. Lévy and W. L. Williams (unpublished).

²⁵A. van Wijngaarden, E. Goh, G. W. F. Drake, and P. S. Farggo, *J. Phys. B* **9**, 2017 (1976).

²⁶D. A. Shiner and L. P. Lévy (unpublished).

²⁷M. A. Player and P. G. H. Sandars, *J. Phys. B* **3**, 1620 (1970); G. E. Harrison, M. A. Player, and P. G. H. Sandars, *J. Phys. E* **4**, 750 (1971).

²⁸A preliminary report appeared in L. P. Lévy and W. L. Williams, *Phys. Rev. Lett.* **48**, 607 (1982).

²⁹In our work to date, mechanical restrictions forbade the operation $\varphi \rightarrow -\varphi$.

³⁰R. T. Robiscoe, *Phys. Rev.* **168**, 4 (1968). There is also a limit on the $2^2S_{1/2} - 2^2P_{1/2}$ mixing in $^4\text{He}^+$ which is ≈ 2000 times larger than our result, and is sensitive to the electron axial vector–nucleon vector coupling; see E. A. Hinds, J. E. Clendenin, and R. Novik, *Phys. Rev. A* **17**, 670 (1978).